Shifting melt composition linked to volcanic tremor at Cumbre Vieja volcano

Marc-Antoine Longpré[1,2,*], Samantha Tramontano[2,1,3], Matthew J. Pankhurst[4,5], Diana C. Roman[6], Miriam C. Reiss[7], Franco Cortese[2,1], Mike R. James[8], Laura Spina[9], Fátima Rodríguez[4], Beverley Coldwell[4,10], Alba Martín-Lorenzo[4,10], Olivia Barbee[4], Luca D'Auria[4,10], Katy J. Chamberlain[11], Jane H. Scarrow[12]

[1]School of Earth and Environmental Sciences, Queens College, City University of New York, Queens, USA
[2]Earth and Environmental Sciences, The Graduate Center, City University of New York, New York, USA
[3]Department of Earth and Planetary Sciences, American Museum of Natural History, New York, USA
[4]Instituto Volcanológico de Canarias, Puerto de la Cruz, Spain
[5]Gaiaxiom, Copenhagen, Denmark
[6]Earth and Planets Laboratory, Carnegie Institution for Science, Washington, DC, USA
[7]Department of Geosciences, Gutenberg University of Mainz, Mainz, Germany
[8]Lancaster Environment Centre, Lancaster University, Lancaster, UK
[9]Istituto Nazionale di Geofisica e Vulcanologia, Sezione di Roma1, Rome, Italy
[10]Instituto Tecnológico y de Energías Renovables, Granadilla de Abona, Spain
[11]School of Environmental Sciences, University of Liverpool, Liverpool, UK
[12]Departamento de Mineralogía y Petrología, Universidad de Granada, Granada, Spain

*correspondence: mlongpre@qc.cuny.edu

Forecasting the onset, evolution, and end of volcanic eruptions relies on interpretation of monitoring data — particularly seismic signals, such as persistent volcanic tremor — in relation to causative magmatic processes. Petrology helps establish such links retrospectively but typically lacks the required temporal resolution to directly relate to geophysical data. Here we report major and volatile element compositions of glass from volcanic ash continuously sampled throughout the 2021 Tajogaite eruption of Cumbre Vieja volcano, La Palma, Canary Islands. The data reveal the evolving chemistry of melts supplied from depth at a daily temporal resolution. Erupted melt compositions become progressively more primitive until the tenth week of activity, but a sharp reversal of this trend then marks the decline of mantle magma supply and a precursory signal to the eruption end. We find that melt SiO_2 content is positively correlated with the amplitude of narrow-band volcanic tremor. Tremor characteristics, inferences from simulations, and model calculations point to melt viscosity-controlled degassing dynamics generating variations in tremor amplitude. Our results show promise for a monitoring and forecasting tool capable of quickly identifying rejuvenated and waning phases of volcanic eruptions and illustrate how subtle changes in melt composition may translate to large shifts in geophysical signals.

Progress in volcano monitoring and forecasting the onset, style, and duration of volcanic eruptions depends on the improved integration and interpretation of multi-disciplinary datasets[1,2]. It remains challenging, however, to directly relate geophysical and geochemical signals observed at the surface to causative processes occurring in inaccessible magmatic systems. For instance, volcanic tremor — an umbrella term for different subclasses of persistent seismic and/or acoustic signals that accompany most volcanic eruptions — is an important parameter in volcano monitoring, yet its source mechanisms have long been unclear[3–6]. Volcanic tremor is typically attributed to interactions between magmatic fluids and the conduit walls at depths ranging from the surface to 40 km[3–9]. At several basaltic volcanoes, the temporal association between eruption and tremor[10–12], tremor source locations[13], and gas data[9] indicate that the dynamics of shallow

magma degassing may drive tremor. Nevertheless, due to the signal complexity, an exact source mechanism for volcanic tremor at mafic systems remains elusive, and multi-disciplinary observations are required to yield novel insight[13].

Petrology, based on the textural and chemical characterization of solid volcanic products, provides key information on the nature and timescales of magmatic processes leading to eruptions[14–16] and on the configuration and dynamics of sub-volcanic magmatic systems[17–19]. Yet petrological approaches have traditionally been too slow and have lacked the temporal resolution required to inform syn-eruptive monitoring or make robust causative links to physical processes. However, thanks to recent technological, methodological, and procedural advances, petrological monitoring can now yield detailed time-series and, rarely, near-real-time data, directly contributing to eruption forecasting,

hazard assessment, and decision making during volcanic episodes[20–23]. Linking temporally-resolved petrological data with real-time geophysical and observational data is likely to contribute future advances in volcano monitoring.

After 50 years of repose and four years of unrest, Cumbre Vieja volcano — a shield volcano featuring a single rift zone and forming the southern half of La Palma, Canary Islands — erupted from 19 September to 13 December 2021[24,25] (Fig. 1a). The eruption occurred upslope of densely populated areas, forcing the evacuation of thousands of residents. Over 85 days, lava flows covered 12.4 km^2 of land, destroying ~3000 buildings, vast plantations, and 92 km of road[26]. Early clinopyroxene–amphibole tephrite lavas with comparatively high viscosities quickly gave way to low-viscosity clinopyroxene–olivine basanites[22,27–30]. The new monogenetic vent system formed a 200-m-high cinder cone, Volcán de Tajogaite, producing near-continuous violent Strombolian explosive activity[31,32]. Ash plumes, averaging ~3 km height and reaching up to ~8 km, blanketed the area with thick tephra[33,34]. The eruption was well-monitored through a variety of ground-based and remote-sensing techniques[31,35–41], and a combination of the nature of the activity and good site accessibility allowed extensive sampling of volcanic products, presenting an exceptional opportunity to integrate geophysical and petrological monitoring[22,28,30,42–44].

A daily time series of melt composition

We conducted systematic sampling of tephra — mostly ash, with some lapilli — during the entirety of the 2021 eruption with the goal of comparing the composition of erupted products with monitoring data and eruptive parameters at a near-daily temporal resolution. A particularly well-located sampling station (AS3), situated directly downwind of the main plume dispersal axis, yielded most samples (Fig. 1, Methods). Our 85 samples and four duplicates each span 28 hours of eruptive activity on average and collectively capture 94% of the eruptive sequence (Table S1). For each sample, ten representative ash particles were picked under a stereomicroscope, mounted in epoxy, and polished.

Two main ash types are observed. Type A ash clasts have fluidal shapes and a vitreous luster, with scanning electron microscopy revealing abundant and variably vesicular glass containing dispersed microcrysts of plagioclase, clinopyroxene, olivine, and Fe-Ti oxides (Fig.

2a,c). In comparison, Type B ash fragments show a similar mineralogy but have a dull to submetallic luster and a nearly glass-free, microcrystalline groundmass with little pore space (Fig. 2b,c). We interpret Type A ash to be of primary juvenile origin, i.e., deriving directly from erupting magma[45]. Conversely, features of Type B ash suggest these clasts underwent high-temperature modifications after initial fragmentation and constitute recycled juvenile particles, consistent with field observations[31], experimental results[46], and textural data at other mafic volcanoes[47]. Therefore, in addition to lacking sufficient glass for direct quantification of quenched melt composition, Type B ash may represent eruptive phases preceding its sampling; we thus focused chemical analysis on Type A ash.

The major and volatile (S, Cl) element compositions of tephra glasses were measured via electron probe micro-analysis on 3–13 spots on at least two distinct Type A ash clasts per sample, totaling 510 data points. After a standard-based correction and averaging for each sample (Methods, Tables S2–S4), the Tajogaite glasses show tephritic to phonotephritic compositions, with 44.8–49.0 wt.% SiO$_2$, 6.3–9.1 wt.% total alkalis (Na$_2$O + K$_2$O), and 3.2–4.7 wt.% MgO, which are generally more silicic, more alkaline, and less magnesian than bulk rocks[28,30] (Fig. 2d,f). Three main features characterize the temporal evolution of glass chemistry during the 2021 eruption (Fig. 2e,g,i). Firstly, a sharp increase in SiO$_2$ concentrations, coupled to a decrease in CaO and FeO$_t$, occurs on 21 September, within two days of eruption onset. Secondly, from 21 September until 29 November, SiO$_2$ progressively decreases, while CaO and FeO$_t$ increase. Thirdly, on 30 November, an inflection point marks the reversal of these trends until the eruption end. In detail, the silica content displays more subtle variations, with six apparent inflection points (Fig. 2e). Other elements (Al$_2$O$_3$, Na$_2$O, K$_2$O, S, and Cl) generally track SiO$_2$, or follow CaO and FeO$_t$ (MgO and TiO$_2$) (Extended Data Figs. 1, 2). Notably, tephra glasses show much wider compositional ranges than bulk lavas for most elements, and temporal trends in tephra glass and bulk lava compositions are strongly decoupled for some (e.g., SiO$_2$ and FeO$_t$)[28,30].

The observed glass composition variations may reflect changes in supplied melt composition, different extents of late-stage crystallization, or both. To assess this, we conducted quantitative textural analysis on 19 ash clasts spanning most of the temporal–

compositional range (Methods, Extended Data Fig. 3, Table S5). Crystallinity ranges from 19 to 43 vol.%, dominated by plagioclase and clinopyroxene, with smaller amounts of Fe-Ti oxide and olivine. Yet, glass composition lacks correlation with the vesicle-free volume fraction of microcrysts (Fig. 2h). Furthermore, mass balance calculations, starting from the most mafic glass and simulating up to 10% crystallization of major mineral phases, demonstrate that the compositional range cannot be produced by crystallization of the observed microcryst assemblage (Fig. 2d,f). This indicates that changes in glass composition relate to actual variations in the composition of melt supplied from depth to the surface over time, consistent with data on lava matrix[42].

These distinct melts may have originated from discrete sources and/or be related through magmatic processes, particularly fractional crystallization[22,28,30] and melt mixing[19,42]. Based on the occurrence of two distinct groups of lavas (Fig. 2d,f and Extended Data Fig. 1)[28,30] and the ubiquitous presence of reversely zoned phenocrysts[42,43,48], we envisage a magma plumbing model similar to those presented elsewhere[22,28,30,42,43]. Rising primitive basanite magma, crystallizing olivine and clinopyroxene, intersected a more evolved clinopyroxene–amphibole-bearing magma body[22] at lower crustal or Moho depths, mobilizing it to erupt. Initially, more silicic melts from the evolved magma body dominated. Subsequently, gradual evacuation of a zoned magma reservoir at mantle depth — established during volcanic unrest through both mixing and fractional crystallization — yielded the eruption of increasingly primitive melts until 30 November. Finally, we interpret the sharp inflection point on 30 November to record the cessation of mantle magma supply; increasingly silicic melts tapped thereafter may represent residual melts temporarily stored in the mid to upper parts of the plumbing system. In hindsight, we contend that this composition trend reversal — subdued in the bulk rock[28,30] and lava matrix[42] data (Fig. 2, Extended Data Fig. 1) — forewarned of the approaching eruption end, as suggested by Ubide et al.[42].

Linkages between melt composition and seismic signals

The high temporal resolution of our dataset enables direct comparison with geophysical monitoring data, such as volcanic earthquakes[36,38] (Methods), which serve as a proxy for magma mobilization at depth[49,50] (Fig. 3a). During the eruption's first week, earthquakes were subdued and shallow (<10 km), but from 1 October onward, hypocenters show a bimodal depth distribution, with clusters at mantle (23 ± 2 km, 1σ) and crustal (9 ± 2 km) depths. While the number of earthquakes and melt composition are not linearly correlated (Fig. 3c), peaks in crustal seismicity often align with breaks in slope in melt composition evolution (Fig. 3a). This is particularly evident on 30 November, where the inflection in melt chemistry coincides with both a spike in crustal seismicity and structural changes at the eruptive vents[40,51].

The mantle and crustal earthquake clusters display a similar but offset sequence of peaks with matching relative amplitudes, suggesting a connection and a time lag between mantle and crustal earthquake swarms, as proposed by Zanon et al.[44]. Assuming this time lag — 13.7–14.8 days in October and 5.7–8.0 days in November and December (Fig. 3a) — reflects magma ascent over the vertical distance between earthquake clusters (13.9 ± 2.6 km), we calculate mantle–crust magma ascent rates of ~0.01 m/s in October and 0.02–0.03 m/s subsequently (Fig. 3d, Methods) (cf. ref. [44]). We thus propose, based on these observations and our glass data, that peaks in earthquakes at 9 ± 2 km depth reflect the arrival, in the crust, of distinct melt pulses[42] supplied from the mantle. The lack of lag between crustal earthquake swarms and melt composition shifts (Fig. 3a) may indicate that magma ascent in the crust occurred within the temporal resolution of our sampling, i.e., in ~1 day (~0.10 m/s, over 9 km), consistent with expected magma acceleration at shallow levels.

We next compare the temporal evolution of melt composition with the amplitude of volcanic tremor (Methods, Fig. 3a, Table S6), a proxy for magma flow and degassing in the shallow conduit[9,13]. The tremor, confined to a narrow 1–3 Hz frequency band at our reference seismic station (PLPI, Fig. 1, Extended Data Fig. 4), surges from hundreds to >10,000 counts at the eruption onset. Unlike discrete earthquakes, the tremor peaks in the first week of activity, then sharply declines on 27 September during a 10-hour eruption lull. Amplitudes gradually rise through October, decline in early November, and show two brief increases on 16–21 November and 27 November–5 December, simultaneous with crustal earthquake swarms (Fig. 3a). The tremor displays a final short-lived surge on 12–13 December, concomitant with a last, powerful eruptive burst, before subsiding with the eruption end.

Intriguingly, the general form of the volcanic tremor closely parallels that of melt SiO_2 content over time (Figs. 3a, 4). To examine this further, we averaged tremor amplitudes for intervals corresponding to each tephra sampling time spans, confirming a broad positive linear correlation between mean narrow-band tremor amplitude and melt composition (Fig. 3b, Table S7). Regression analysis, with both variables resampled to daily averages and normalized from 0 to 1, yields a correlation coefficient of 0.64 and a p-value below 0.001 (Fig. 4, Extended Data Fig. 5, Table S8), indicating that the null hypothesis — that melt SiO_2 content and tremor amplitude are unrelated — is unlikely. Mismatches between the two time series are mainly associated with crustal earthquake swarms in late October, mid-November, and early December (Figs. 3a, 4), which may be related to tremor bursts.

Our results thus reveal an enigmatic relationship between melt composition and volcanic tremor at Tajogaite. Several tremor generation mechanisms may be invoked, including resonance of a fluid-filled crack and bubble nucleation, coalescence, oscillation, and bursting[4–6,52,53], though none may be *a priori* directly tied to melt composition. However, signal locations performed using open-source data from the Instituto Geográfico Nacional network[54] indicate a stable and shallow tremor source, most likely within the uppermost kilometer of the conduit (Methods, Extended Data Figs. 6–9). Therefore, large amplitude shifts at near-constant frequency throughout the eruptive sequence (Fig. 3a, Extended Data Fig. 4) may reflect pressure variations in this dominant tremor source[3,55].

A melt viscosity control on volcanic tremor

To explore the possible origins of the melt composition–tremor relationship, we turn to laboratory experiments specifically scaled to test the effects of gas flow rate, magma viscosity, and conduit geometry on the degassing behavior and related seismo-acoustic signals at mafic volcanoes[56–58]. These analogue models show that increasing gas flow rate and liquid viscosity drive transitions in gas–liquid flow from bubbly to slug to annular regimes (Fig. 5a), which are typically interpreted as resulting in eruptive styles (e.g., passive degassing, Strombolian, and lava fountaining, respectively)[56] observed at Tajogaite[31,32]. Notably, the models illustrate the positive relationship between gas flow rate and the amplitude of tremor-like pressure signals within and above the gas–liquid mixture (Fig. 5a, Extended Data Fig. 10). Liquid viscosity also

appears to affect the amplitude of analogue tremor; i.e., at high gas flow rate and for a given flow regime, higher liquid viscosity ($>10^2$ Pa s) is associated with greater signal amplitudes (Fig. 5a). Moreover, in slug flow, increased viscosity reduces slug ascent velocity and the recurrence rate of slug bursts and associated discrete seismo-acoustic events[56] (Extended Data Fig. 10). Thus, analogue models point to volume flux — particularly of gas — and melt viscosity as key factors controlling tremor amplitude in mafic systems.

At Tajogaite, magma and gas fluxes are best tracked by time-averaged discharge rate (TADR) estimates from satellite thermal imagery[59] and SO_2 emissions detected by the Sentinel-5P TROPOMI instrument[60], respectively (Fig. 3a). However, while there may be some correspondence between TADR, SO_2, and tremor amplitude[32], we find little evidence for a primary control of magma and gas fluxes on tremor (Fig. 3a, Extended Data Fig. 5, Table S8). Moreover, magmatic volatile contents, though very high, appear to exhibit only slight variations throughout the eruption[61,62] (Extended Data Fig. 2). We also find no correlation between the ash-laden plume height, a coarse proxy for eruptive style and explosivity[33,63], and tremor (Extended Data Fig. 5, Table S8).

In contrast, an influence of melt viscosity on tremor amplitude provides a direct link with our tephra glass data. Indeed, melt composition, particularly SiO_2 and H_2O contents, strongly controls melt viscosity[64]. Laboratory measurements[27,29] yield generally low melt viscosities for the 2021 magmas and align well with values calculated with the model of Giordano et al.[65], which thus appears reasonably accurate for mafic alkaline compositions. Applying this model along with a thermometer[66] to our data, we obtain melt viscosities of 280–2250 Pa s and 10–30 Pa s for anhydrous and hydrous (3 wt.% H_2O) conditions, respectively (Fig. 5b,c) (Methods). We emphasize that these calculations best represent the viscosity of the melt phase, not that of the three-phase magma — although, at the observed range of crystallinities[22,67] (Fig. 2h), the effective viscosity of a crystal–melt mixture is dominated by melt viscosity[68]. At the shallow depths relevant to tremor generation, where initially dissolved water has largely exsolved to a gas phase (Fig. 5b, Extended Data Fig. 2), near-anhydrous melt viscosities are most appropriate[67]. Unsurprisingly, anhydrous viscosity logarithms positively correlate with SiO_2

contents (r = 0.92) and, hence, tremor amplitude (Fig. 5c,d).

Although our data do not pinpoint the tremor generation mechanism, they indicate sensitivity to melt viscosity variations, offering new insights into its origin. We propose that melt composition exerted a first-order control on volcanic tremor at Tajogaite, via effects of melt viscosity on rising and bursting gas bubbles (Fig. 6). Variations in magma and gas flux also likely influenced short-term tremor amplitude increases (Fig. 3a). In addition to being supported by analogue experiments[56], this scenario is substantiated by analytical and numerical models simulating gas slug ascent during Strombolian activity[69–71]. For instance, James et al.[69] showed that a modest increase in melt viscosity — from 300 to 500 Pa s, a range considerably smaller than we calculate for the 2021 anhydrous melts — leads to greater overpressure in rising and bursting gas slugs. Although the complex natural system at Tajogaite — with multiple vents, variable eruptive styles, and a conduit of unknown, and possibly tilted, geometry[31,61,72] — limits quantitative modelling here, the relationships between melt viscosity, bubble ascent speeds, and bubble overpressure are expected to hold true. Higher-SiO_2, higher-viscosity melts were characterized by slower bubble ascent and higher bubble overpressure (and thus lower magma compressibility), causing greater pressure variability in the shallow conduit and, consequently, higher tremor amplitudes.

Frontiers in petrological monitoring

Based on a systematic sampling campaign, our results unveil changes in melt composition during the 2021 Tajogaite eruption at Cumbre Vieja, contributing to an emerging picture of rapidly evolving magma supply during mafic eruptions[20,21]. We suggest the sharp reversal of compositional trends on 30 November marks the waning of mantle-derived magma supply and represents a precursory signal to the eruption's end two weeks later. The daily resolution of our dataset unlocks precise comparison of petrological and geophysical records, revealing an intriguing correlation between melt composition and volcanic tremor amplitude. We propose that this correlation stems from melt viscosity-driven changes in rising and bursting gas bubbles and slugs, affecting overpressure and ascent speed, as supported by existing models[56,69–71]. Similar melt composition and viscosity controls on tremor amplitude may apply to other mafic volcanoes. Our analysis should

provide inspiration for further field, laboratory, and theoretical work aimed at better understanding the source mechanisms of volcanic tremor and improve its forecasting power.

Our work also demonstrates the value of tephra glass composition as a petrological monitoring tool[23,73]. Rapid sample preparation and analysis may be achieved on daily timescales, and results allow identifying subtle changes in melt composition that may be blurred in bulk rock data. Such compositional shifts can aid in interpreting changing geophysical parameters and recognizing rejuvenated or terminal eruption phases, enhancing forecasting efforts[20]. However, coordinating collaborative work and sample transfer during eruptive crises is a major challenge that requires careful pre-planning[23,74]. The near-site deployment of portable X-ray fluorescence spectrometers[20,75] and benchtop scanning electron microscopes, with energy-dispersive X-ray detectors allowing quantitative glass analyses[73], can accelerate workflow and open up new frontiers in petrological monitoring of volcanic eruptions.

Author contributions

M.-A.L., S.T., and M.J.P. conceptualized the study. Field work was carried out by M.J.P., S.T., F.C., F.R., B.C., A.M.-L., O.B., J.H.S, K.J.C., and M.-A.L. Sample preparation and EPMA data collection were performed by S.T., while F.C. conducted image analysis and prepared Extended Data Figure 3. L.D'A. collected and curated the seismic data from the INVOLCAN network. D.C.R. and M.C.R. analyzed tremor data and drafted Extended Data Figures 4, 6–9. M.J.P. prepared Figure 1. Data analysis was undertaken by M.-A.L. and S.T., with M.R.J. and L.S. contributing to data interpretation. M.-A.L. drafted the remaining

figures and wrote the manuscript, with contributions from S.T and all authors.
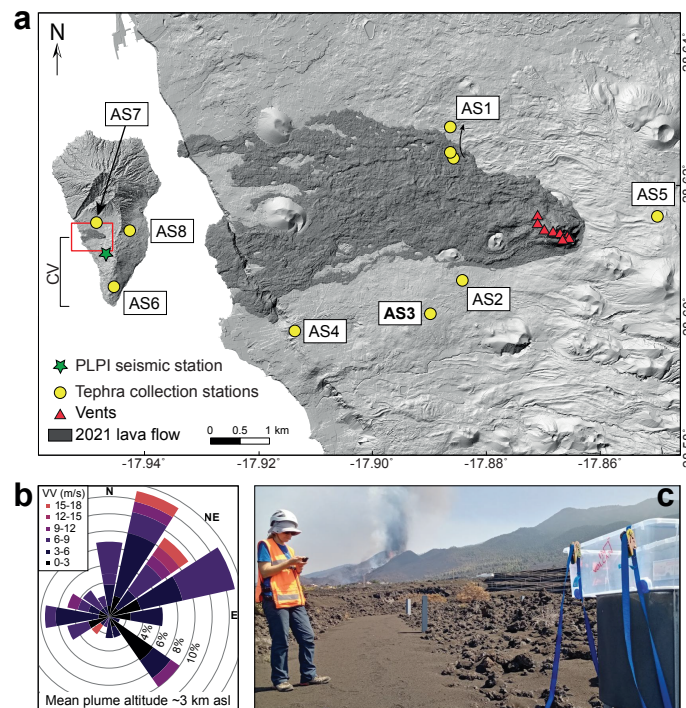
**Figure 1. Map of lava flows and vents of the 2021 Tajogaite eruption at Cumbre Vieja volcano.** (a) Shaded relief map (source: www.grafcan.es) showing the lava flow field, the Tajogaite vents, and the location of continuous tephra collection stations. Inset: The island of La Palma and Cumbre Vieja volcano (CV), with the location of PLPI seismic station, just south of the area enlarged in (a). (b) Wind rose diagram indicating dominant wind directions and speeds (VV, in m/s) at an altitude of 3 km above sea level, close to average ash plume height during the eruption. Note AS3 (bolded), our main sampling station, situated directly downwind from the vent. (c) Photograph of the AS3 field site.
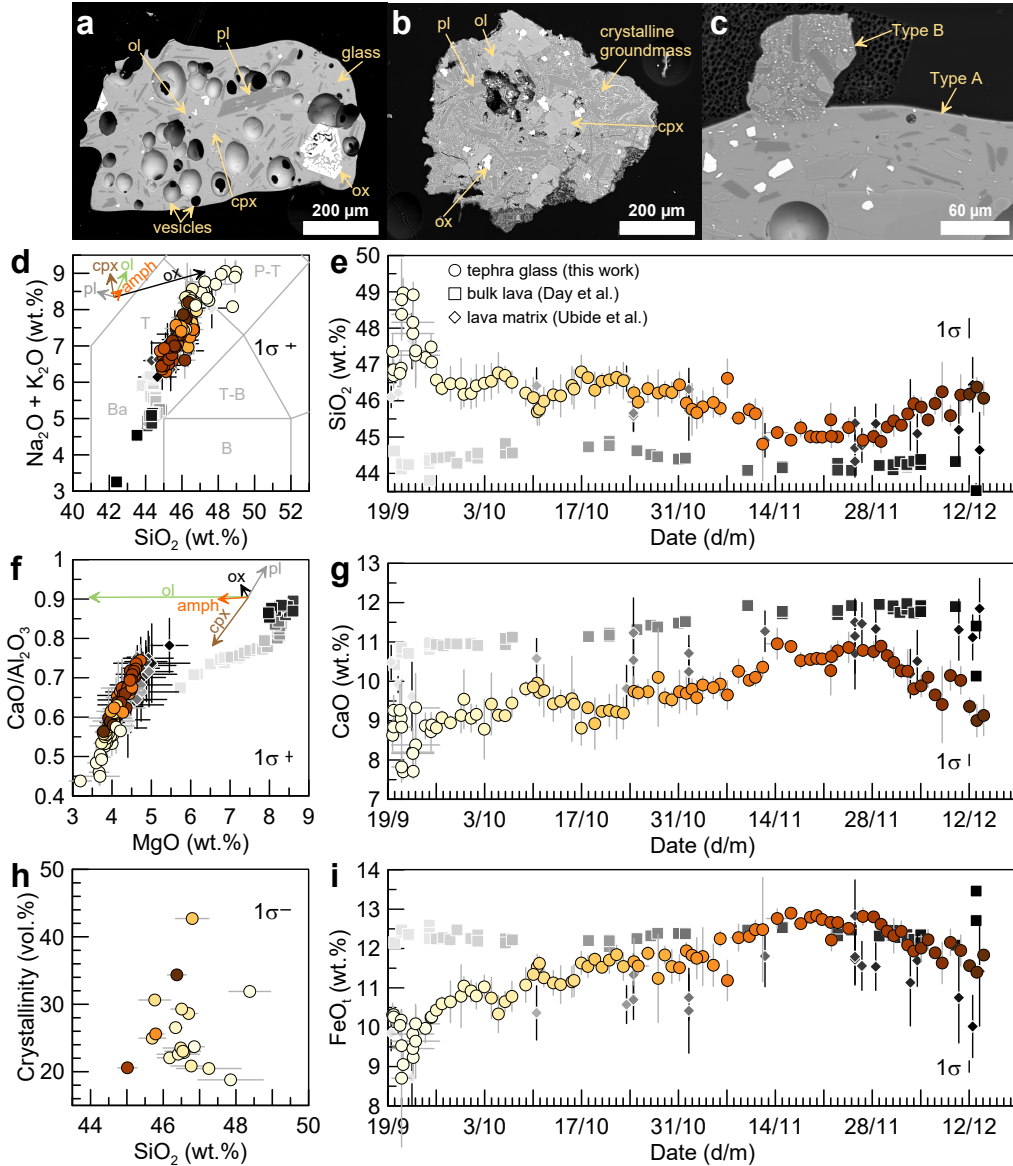
Figure 2. Temporal evolution of melt composition at Tajogaite. Representative backscattered electron images of Type A (glassy, juvenile origin) and Type B (microcrystalline, recycled juvenile origin) ash are shown in (a) and (b), respectively. (c) Type B clast attached to a Type A clast. Mineral abbreviations: Amph, amphibole; Cpx, clinopyroxene; Pl, plagioclase; Ol, olivine; Ox, Fe-Ti oxide. (d–i) Mean glass composition of dated Type A ash (circles) compared to bulk rock[28] and mean lava matrix[42] compositions. (d) Total alkali vs. silica classification diagram. B, basalt; Ba, basanite; T, tephrite; T-B, trachybasalt; P-T , phonotephrite. (e, g, i) SiO_2, CaO, and FeO_t concentrations plotted over time (day/month of 2021, UTC). (f) CaO/Al_2O_3 vs. MgO. (h) Microcryst content (vol.%) vs. SiO_2. Symbol color gradients refer to eruption date, as shown in (e, g, i). Gray error bars show one standard deviation based on 3–13 analyses on at least two ash clasts per sample, with horizontal bars in (e, g, i) indicating ash sampling timespan. Error bars smaller than symbol size are not shown. Thin black error bars labelled 1σ represent the one standard deviation analytical precision based on repeated analyses (n=60) of the P1326-2 glass standard. Black error bars for lava matrix data are one standard deviation from 7–10 analyses[42]. In (d, f), colored arrows represent melt composition shifts due to 10% crystallization of labelled minerals, starting from the most mafic glass. Mineral compositions are from Pankhurst et al.[22], and crystallization vectors are displaced to the upper part of plots for clarity.
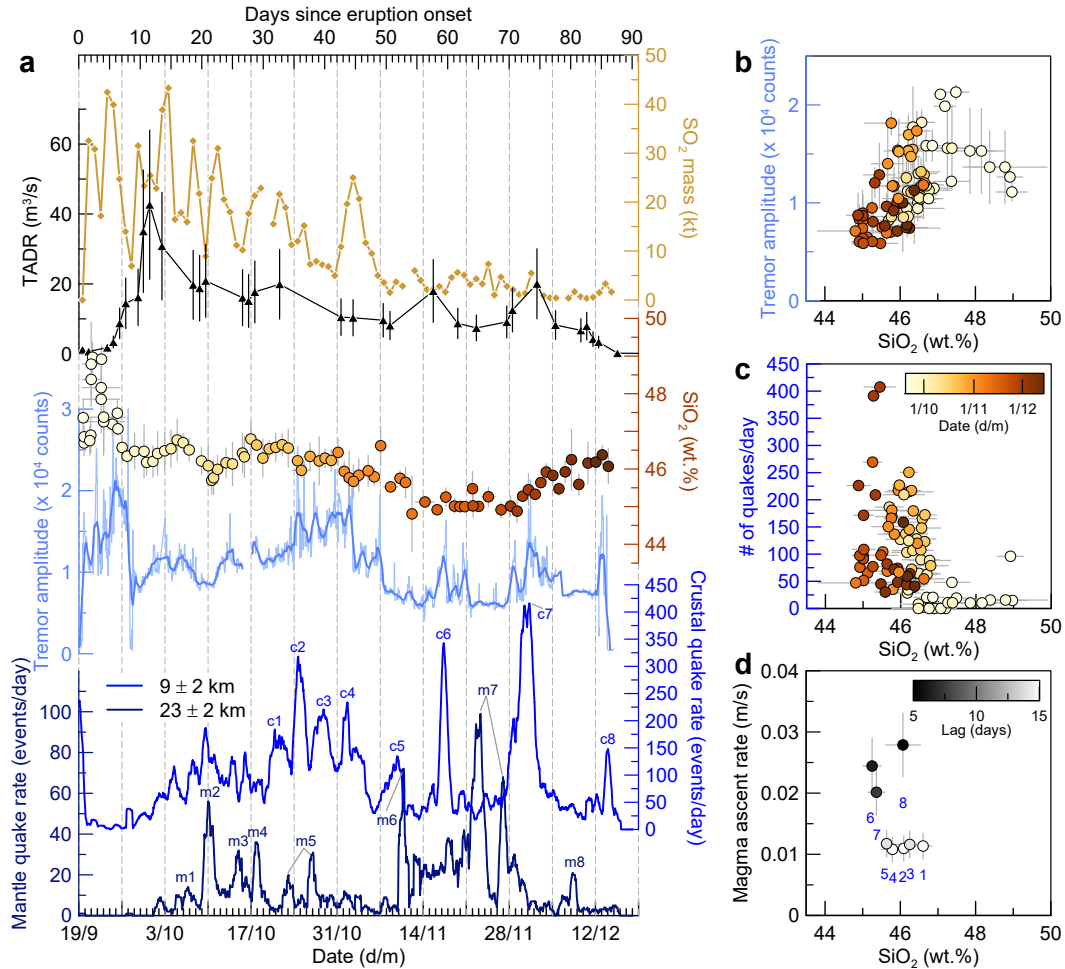
Figure 3. Comparison with monitoring data. (a) Time series of melt SiO_2 content (error bars as in Fig. 2) alongside the discrete seismicity rate (24-hr moving average, 1-hr window) in the mantle (23 ± 2 km, navy blue line) and crustal (9 ± 2 km, blue line) clusters, using data from D'Auria et al.[36]. Labels m_i and c_i denote presumably matching mantle and crustal earthquake swarms separated by time lags of 13.7–14.8 days in October and 5.7–8.0 days in November and December. The volcanic tremor amplitude in the 1–3 Hz band — real-time seismic amplitude measurement (RSAM) at station PLPI (Methods) — is shown as 1-hr average (thin, light blue line) and 24-hr moving average with 1-hr window (thicker, pale blue line). Time-averaged discharge rate (TADR) estimates (with ±50% error bars)[59] and Sentinel-5P TROPOMI SO_2 emissions[60] are also shown as proxies of magma and gas fluxes, respectively. Vertical gray dashed lines indicate weekly intervals. (b) Mean tremor amplitude and (c) seismicity rate (earthquakes per day) during each tephra collection period versus corresponding melt SiO_2 content. (d) Estimated mantle–crust magma ascent rates (based on lags between the eight mantle–crust earthquake swarm pairs shown in (a)) versus melt SiO_2 content at the time of corresponding peak crustal seismicity. Error bars for tremor amplitude and SiO_2 in (b–d) show one standard deviation, while magma ascent rate error bars reflect the propagated uncertainty in the vertical distance between the two earthquake clusters.
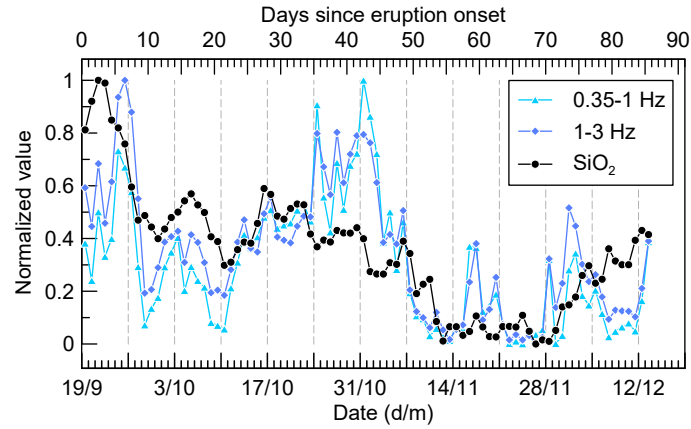
Figure 4. Normalized time series. Resampled (daily averages) and normalized [0, 1] time series of melt SiO_2 content and tremor amplitude in the 1–3 Hz and 0.35–1 Hz bands recorded at station PLPI. Both tremor time series show a statistically significant correlation with melt SiO_2 content (Extended Data Fig. 5, Table S8). Vertical gray dashed lines indicate weekly intervals.
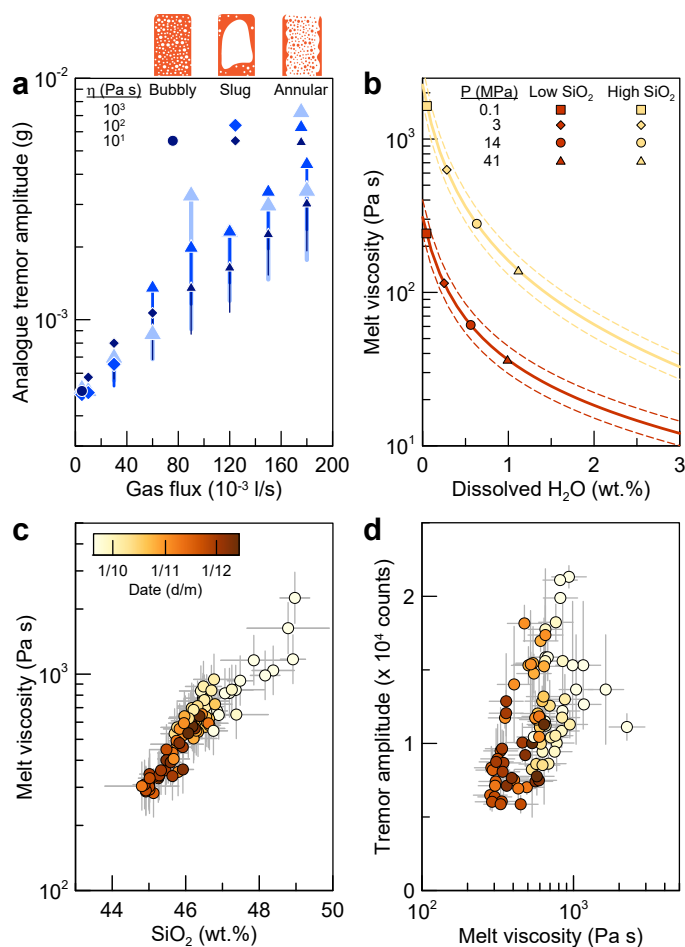
Figure 5. Effects of melt viscosity. (a) Amplitude of analogue tremor as a function of gas flux in laboratory experiments[56]. Symbols indicate the average 75th percentile values for three experiments (230–525 observations per experiment, over 46–105 s using a 0.2 s sliding window) conducted with different conduit roughness, with downward error bars representing the average interquartile range. Colors correspond to liquid viscosity (η) in the experiments, and symbol shapes denote the observed flow regime (bubbly, slug, or annular, illustrated in cartoons above where melt is orange and gas is white — modified after ref. [76]). (b) Calculated melt viscosity versus dissolved H_2O content for low- and high-SiO_2 melt endmembers (respectively, 44.9 and 49.0 wt.% SiO_2) at Tajogaite. Symbols indicate calculated H_2O solubility at pressures of 0.1, 3, 14, and 41 MPa, corresponding to depths of approximately 0, 100, 500, and 1500 m in the conduit (assuming a magma density of 2800 kg/m³). Uncertainty envelopes shown by dashed lines consider an error of ±10°C on temperature[66], plus a 5% error of the viscosity model[65]. (c) Anhydrous melt viscosity versus SiO_2 content for all samples, and (d) tremor amplitude as a function of anhydrous melt viscosity. Viscosity error bars in (c) and (d) were calculated as in (b).
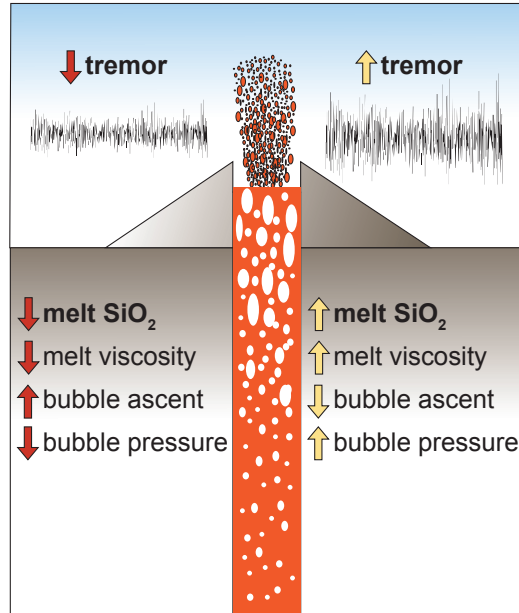
Figure 6. Conceptual model. Schematic illustration summarizing the proposed effect of melt viscosity on tremor amplitude. Comparatively high melt SiO_2 translates into higher melt viscosity, slower bubble ascent velocity, and higher overpressure in rising gas bubbles and slugs, together yielding higher amplitude of shallow tremor.

References

1. Bebbington, M. S. & Jenkins, S. F. Intra-eruption forecasting. *Bulletin of Volcanology* **81**, 1–17 (2019).

2. Poland, M. P. & Anderson, K. R. Partly cloudy with a chance of lava flows: Forecasting volcanic eruptions in the twenty-first century. *Journal of Geophysical Research: Solid Earth* **125**, e2018JB016974 (2020).

3. Benoit, J. P., McNutt, S. R. & Barboza, V. Duration-amplitude distribution of volcanic tremor. *Journal of Geophysical Research: Solid Earth* **108**, 2146 (2003).

4. Chouet, B. Excitation of a buried magmatic pipe: a seismic source model for volcanic tremor. *Journal of Geophysical Research: Solid Earth* **90**, 1881–1893 (1985).

5. Girona, T., Caudron, C. & Huber, C. Origin of shallow volcanic tremor: the dynamics of gas pockets trapped beneath thin permeable media. *Journal of Geophysical Research: Solid Earth* **124**, 4831–4861 (2019).

6. Konstantinou, K. I. & Schlindwein, V. Nature, wavefield properties and source mechanism of volcanic tremor: a review. *Journal of Volcanology and Geothermal Research* **119**, 161–187 (2003).

7. Fee, D. *et al.* Volcanic tremor and plume height hysteresis from Pavlof Volcano, Alaska. *Science* **355**, 45–48 (2017).

8. McNutt, S. R. Volcanic tremor amplitude correlated with eruption explosivity and its potential use in determining ash hazards to aviation. in *Volcanic Ash and Aviation Safety: Proceedings of the First International Symposium on Volcanic Ash and Aviation Safety* vol. 2047 377–385 (1994).

9. Salerno, G. G., Burton, M., Di Grazia, G., Caltabiano, T. & Oppenheimer, C. Coupling between magmatic degassing and volcanic tremor in basaltic volcanism. *Frontiers in Earth Science* **6**, 157 (2018).

10. Alparone, S., Andronico, D., Lodato, L. & Sgroi, T. Relationship between tremor and volcanic activity during the Southeast Crater eruption on Mount Etna in early 2000. *Journal of Geophysical Research: Solid Earth* **108**, (2003).

11. Battaglia, J., Aki, K. & Ferrazzini, V. Location of tremor sources and estimation of lava output using tremor source amplitude on the Piton de la Fournaise volcano: 1. Location of tremor sources. *Journal of Volcanology and Geothermal Research* **147**, 268–290 (2005).

12. Soubestre, J., Chouet, B. & Dawson, P. Sources of volcanic tremor associated with the summit caldera collapse during the 2018 east rift eruption of Kīlauea Volcano, Hawai'i. *Journal of Geophysical Research: Solid Earth* **126**, e2020JB021572 (2021).

13. Journeau, C. *et al.* Tracking changes in the co-eruptive seismic tremor associated with magma degassing at Piton de la Fournaise volcano. *Journal of Volcanology and Geothermal Research* **444**, 107936 (2023).

14. Costa, F., Shea, T. & Ubide, T. Diffusion chronometry and the timescales of magmatic processes. *Nature Reviews Earth & Environment* 1–14 (2020).

15. Kahl, M., Chakraborty, S., Costa, F. & Pompilio, M. Dynamic plumbing system beneath volcanoes revealed by kinetic modeling, and the connection to monitoring data: An example from Mt. Etna. *Earth and Planetary Science Letters* **308**, 11–22 (2011).

16. Pankhurst, M. J., Morgan, D. J., Thordarson, T. & Loughlin, S. C. Magmatic crystal records in time, space, and process, causatively linked with volcanic unrest. *Earth and Planetary Science Letters* **493**, 231–241 (2018).

17. Cashman, K. V., Sparks, R. S. J. & Blundy, J. D. Vertically extensive and unstable magmatic systems: a unified view of igneous processes. *Science* **355**, eaag3055 (2017).

18. Ganne, J., Bachmann, O. & Feng, X. Deep into magma plumbing systems: Interrogating the crystal cargo of volcanic deposits. *Geology* **46**, 415–418 (2018).

19. Longpré, M.-A., Klügel, A., Diehl, A. & Stix, J. Mixing in mantle magma reservoirs prior to and during the 2011–2012 eruption at El Hierro, Canary Islands. *Geology* **42**, 315–318 (2014).

20. Gansecki, C. *et al.* The tangled tale of Kīlauea's 2018 eruption as told by geochemical monitoring. *Science* **366**, 1212 (2019).

21. Halldórsson, S. A. *et al.* Rapid shifting of a deep magmatic source at Fagradalsfjall volcano, Iceland. *Nature* **609**, 529–534 (2022).

22. Pankhurst, M. J. *et al.* Rapid response petrology for the opening eruptive phase of the 2021 Cumbre Vieja eruption, La Palma, Canary Islands. *Volcanica* **5**, 1–10 (2022).

23. Re, G., Corsaro, R. A., D'Oriano, C. & Pompilio, M. Petrological monitoring of active volcanoes: A review of existing procedures to achieve best practices and operative protocols during eruptions. *Journal of Volcanology and Geothermal Research* **419**, 107365 (2021).

24. Carracedo, J. C. *et al.* The 2021 eruption of the Cumbre Vieja volcanic ridge on La Palma, Canary Islands. *Geology Today* **38**, 94–107 (2022).

25. Longpré, M.-A. Reactivation of Cumbre Vieja volcano. *Science* **374**, 1197–1198 (2021).

26. Copernicus Emergency Management Service (© 2021 European Union). *EMSR546* https://emergency.copernicus.eu/mapping/list-of-components/EMSR546 (2021).

27. Castro, J. M. & Feisel, Y. Eruption of ultralow-viscosity basanite magma at Cumbre Vieja, La Palma, Canary Islands. *Nature Communications* **13**, 3174 (2022).

28. Day, J. M. *et al.* Mantle source characteristics and magmatic processes during the 2021 La Palma eruption. *Earth and Planetary Science Letters* **597**, 117793 (2022).

29. Di Fiore, F. *et al.* Experimental constraints on the rheology of lavas from 2021 Cumbre Vieja eruption (La Palma, Spain). *Geophysical Research Letters* **50**, e2022GL100970 (2023).

30. Scarrow, J. H. *et al.* Decoding links between magmatic processes and eruption dynamics: whole-rock time series petrology of the 2021 Tajogaite eruption, La Palma. *Volcanica* (in press).

31. Taddeucci, J. *et al.* The explosive activity of the 2021 Tajogaite eruption (La Palma, Canary Islands, Spain). *Geochemistry, Geophysics, Geosystems* **24**, e2023GC010946 (2023).

32. Birnbaum, J. *et al.* Temporal variability of explosive activity at Tajogaite volcano, Cumbre Vieja (Canary Islands), 2021 eruption from ground-based infrared photography and videography. *Frontiers in Earth Science* **11**, 1193436 (2023).

33. Bonadonna, C. *et al.* Physical characterization of long-lasting hybrid eruptions: The 2021 Tajogaite eruption of Cumbre Vieja (La Palma, Canary Islands). *Journal of Geophysical Research: Solid Earth* **127**, e2022JB025302 (2022).

34. Romero, J. E. *et al.* The initial phase of the 2021 Cumbre Vieja ridge eruption (Canary Islands): Products and dynamics controlling edifice growth and collapse. *Journal of Volcanology and Geothermal Research* **431**, 107642 (2022).

35. Civico, R. *et al.* High-resolution digital surface model of the 2021 eruption deposit of Cumbre Vieja volcano, La Palma, Spain. *Scientific Data* **9**, 435 (2022).

36. D'Auria, L. *et al.* Rapid magma ascent beneath La Palma revealed by seismic tomography. *Scientific Reports* **12**, 17654 (2022).

37. De Luca, C. *et al.* Pre-and co-eruptive analysis of the September 2021 eruption at Cumbre Vieja volcano (La Palma, Canary Islands) through DInSAR measurements and analytical modeling. *Geophysical Research Letters* **49**, e2021GL097293 (2022).

38. Del Fresno, C. *et al.* Magmatic plumbing and dynamic evolution of the 2021 La Palma eruption. *Nature Communications* **14**, 358 (2023).

39. Román, A. *et al.* Unmanned aerial vehicles (UAVs) as a tool for hazard assessment: The 2021 eruption of Cumbre Vieja volcano, La Palma Island (Spain). *Science of the Total Environment* **843**, 157092 (2022).

40. Walter, T. R. *et al.* Late complex tensile fracturing interacts with topography at Cumbre Vieja, La Palma. *Volcanica* **6**, 1–17 (2023).

41. Weisz, E. & Menzel, W. P. Monitoring the 2021 Cumbre Vieja volcanic eruption using satellite multisensor data fusion. *Journal of Geophysical Research: Atmospheres* **128**, e2022JD037926 (2023).

42. Ubide, T. *et al.* Discrete magma injections drive the 2021 La Palma eruption. *Science Advances* **9**, eadg4813 (2023).

43. Dayton, K. *et al.* Deep magma storage during the 2021 La Palma eruption. *Science Advances* **9**, eade7641 (2023).

44. Zanon, V., D'Auria, L., Schiavi, F., Cyrzan, K. & Pankhurst, M. J. Toward a near real-time magma ascent monitoring by combined fluid inclusion barometry and ongoing seismicity. *Science Advances* **10**, eadi4300 (2024).

45. White, J. D. L. & Houghton, B. F. Primary volcaniclastic rocks. *Geology* **34**, 677–680 (2006).

46. D'Oriano, C., Pompilio, M., Bertagnini, A., Cioni, R. & Pichavant, M. Effects of experimental reheating of natural basaltic ash at different temperatures and redox conditions. *Contributions to Mineralogy and Petrology* **165**, 863–883 (2013).

47. D'Oriano, C., Bertagnini, A., Cioni, R. & Pompilio, M. Identifying recycled ash in basaltic eruptions. *Scientific Reports* **4**, 5851 (2014).

48. Tramontano, S. Untangling the Nature and Timescales of Magmatic Processes Driving Eruptions at Quiescent Volcanoes: Examples from Driving Eruptions at Quiescent Volcanoes: Examples from Momotombo, Nicaragua, and Cumbre Vieja, Canary Islands, PhD thesis, City University of New York. (2023).

49. McNutt, S. R. Seismic Monitoring and Eruption Forecasting of Volcanoes: A Review of the State-of-the-Art and Case Histories. *Monitoring and Mitigation of Volcano Hazards* 99–146 (1996).

50. Roman, D. C. & Cashman, K. V. The origin of volcano-tectonic earthquake swarms. *Geology* **34**, 457–460 (2006).

51. González, P. J. Volcano-tectonic control of Cumbre Vieja. *Science* **375**, 1348–1349 (2022).

52. Ripepe, M. & Gordeev, E. Gas bubble dynamics model for shallow volcanic tremor at Stromboli. *Journal of Geophysical Research: Solid Earth* **104**, 10639–10654 (1999).

53. Palma, J. L., Calder, E. S., Basualto, D., Blake, S. & Rothery, D. A. Correlations between SO2 flux, seismicity, and outgassing activity at the open vent of Villarrica volcano, Chile. *Journal of Geophysical Research: Solid Earth* **113**, (2008).

54. Instituto Geografico Nacional, Spain. Spanish Digital Seismic Network. (1999) doi:10.7914/SN/ES.

55. Ripepe, M. *et al.* Seismic and infrasonic evidences for an impulsive source of the shallow volcanic tremor at Mt. Etna, Italy. *Geophysical Research Letters* **28**, 1071–1074 (2001).

56. Spina, L., Cannata, A., Morgavi, D. & Perugini, D. Degassing behaviour at basaltic volcanoes: New insights from experimental investigations of different conduit geometry and magma viscosity. *Earth-Science Reviews* **192**, 317–336 (2019).

57. Spina, L., Morgavi, D., Cannata, A., Campeggi, C. & Perugini, D. An experimental device for characterizing degassing processes and related elastic fingerprints: Analog volcano seismo-acoustic observations. *Review of Scientific Instruments* **89**, (2018).

58. Spina, L., Cannata, A., Morgavi, D., Privitera, E. & Perugini, D. Seismo-acoustic gliding: An experimental study. *Earth and Planetary Science Letters* **579**, 117344 (2022).

59. Plank, S. *et al.* Combining thermal, tri-stereo optical and bi-static InSAR satellite imagery for lava volume estimates: the 2021 Cumbre Vieja eruption, La Palma. *Scientific Reports* **13**, 2057 (2023).

60. Global Sulfur Dioxide Monitoring. https://so2.gsfc.nasa.gov/.

61. Burton, M. *et al.* Exceptional eruptive CO2 emissions from intra-plate alkaline magmatism in the Canary volcanic archipelago. *Communications Earth & Environment* **4**, 467 (2023).

62. Dayton, K. *et al.* Magmatic storage and volatile fluxes of the 2021 La Palma eruption. *Geochemistry, Geophysics, Geosystems* **25**, e2024GC011491 (2024).

63. Toulouse Volcanic Ash Advisory Centre. La Palma. http://vaac.meteo.fr/volcanoes/la-palma/. Volcanic Ash Advisory Centre Toulouse (2021).

64. Lesher, C. E. & Spera, F. J. Thermodynamic and transport properties of silicate melts and magma. in *The Encyclopedia of Volcanoes* (eds. Sigurdsson, H., Houghton, B., McNutt, S. R., Rymer, H. & Stix, J.) 113–141 (Elsevier, 2015).

65. Giordano, D., Russell, J. K. & Dingwell, D. B. Viscosity of magmatic liquids: A model. *Earth and Planetary Science Letters* **271**, 123–134 (2008).

66. Beattie, P. Olivine-melt and orthopyroxene-melt equilibria. *Contributions to Mineralogy and Petrology* **115**, 103–111 (1993).

67. Gisbert, G. *et al.* Reported ultra-low lava viscosities from the 2021 La Palma eruption are potentially biased. *Nature Communications* **14**, 6453 (2023).

68. Shamloo, H. & Kent, A. An appraisal of the observed crystallinities of volcanic materials. *Volcanica* **7**, 105–115 (2024).

69. James, M. R., Lane, S. J. & Corder, S. B. Modelling the rapid near-surface expansion of gas slugs in low-viscosity magmas. *Geological Society, London, Special Publications* **307**, 147–167 (2008).

70. James, M. R., Lane, S. J., Wilson, L. & Corder, S. B. Degassing at low magma-viscosity volcanoes: Quantifying the transition between passive bubble-burst and Strombolian eruption. *Journal of Volcanology and Geothermal Research* **180**, 81–88 (2009).

71. Del Bello, E., Llewellin, E. W., Taddeucci, J., Scarlato, P. & Lane, S. J. An analytical model for gas overpressure in slug-driven explosions: Insights into Strombolian volcanic eruptions. *Journal of Geophysical Research: Solid Earth* **117**, (2012).

72. Przeor, M. *et al.* Geodetic imaging of magma ascent through a bent and twisted dike during the Tajogaite eruption of 2021 (La Palma, Canary Islands). *Scientific Reports* **14**, 212 (2024).

73. Corsaro, R. A. & Miraglia, L. Near real-time petrologic monitoring on volcanic glass to infer magmatic processes during the February–April 2021 paroxysms of the South-East Crater, Etna. *Frontiers in Earth Science* (2022).

74. Cooper, K. M. *et al.* Coordinating science during an eruption: lessons from the 2020–2021 Kīlauea volcanic eruption. *Bulletin of Volcanology* **85**, 1–13 (2023).

75. Steiner, A. E., Conrey, R. M. & Wolff, J. A. PXRF calibrations for volcanic rocks and the application of in-field analysis to the geosciences. *Chemical Geology* **453**, 35–54 (2017).

76. Gonnermann, H. M. & Manga, M. Dynamics of magma ascent. *Modeling volcanic processes: The physics and mathematics of volcanism* **55**, (2013).

Methods

Samples

Tephra was collected during the 85 days of eruption. The longest sampling gap is ~23 hours on 7 October. In the first few days of eruptive activity, tephra collection was conducted onto plastic sheets and paper containers. However, this ad hoc method was rapidly superseded by systematic sampling using a network of plastic box collection stations, from which samples were retrieved (and stations reset for continuous collection) almost daily. These sampling stations were placed in open spaces and secured with straps, away from roads, and protected from aeolian remobilization. Most samples used in this work come from station AS3 (UTM coordinates, 217550 Easting, 3167233 Northing, zone 28 R, datum WGS84) which was installed on 26 September 2021. AS3 was chosen because: (1) it was located under the tephra plume for most of the eruption duration and thus provides a near-continuous sampling record; and (2) the grain size of its samples is

optimal for selection of representative particles for analysis. Stations closer to the vent show coarser grain sizes that require breaking clasts into smaller pieces for analysis, while finer particles from more distal stations may be biased due to winnowing[22]. For the few days when the tephra plume was oriented away from AS3, we selected tephra from other stations to complement our sample set (Table S1). A total of 85 distinct tephra samples, in addition to 4 duplicate samples, were selected for analysis.

Sample preparation and electron probe micro-analysis

Representative ash clasts (10 for each sample, total ~890) were hand-picked under a stereomicroscope, mounted in 1-inch epoxy disks, and polished. Observations with reflected light and scanning electron microscopes allowed identification of the two broad types of ash particles and selection of Type A clasts (showing fluidal shapes and abundant glass), as representative juvenile particles. Electron probe micro-analysis of glass in Type A clasts was conducted by wavelength-dispersive X-ray spectroscopy on a Cameca SX5-Tactis instrument at the American Museum of Natural History in New York City, over four sessions. Analytical conditions were chosen to prevent migration of alkalis upon electron beam exposure and consisted of an acceleration voltage of 15 kV, a beam current of 10 nA, and a beam diameter of 15 μm. Calibration of the instrument was performed using natural mineral and glass standards. Peak counting times were 10 s for Na and K, 20 s for Al, Mg, Si, P, Ti, Ca, Mn, and Fe, and 30 s for Cl and S. To estimate glass composition variability in each selected dated tephra, we acquired 3–13 data points on at least 2 separate ash clasts per sample, yielding a total of 510 data points.

Repeated analyses of glass standards P1326-2 (n=60)[77], AGV-1 (n=16), and Macusanite (n=45)[78] during our analytical sessions are reported in Table S2 and demonstrate the good precision and accuracy of the data. For instance, based on all P1326-2 data, overall precision (at the one standard deviation level) and accuracy (relative error) are 0.8% and 1.2% for Si and respectively better than 2.3% and 2.7% for all elements present in concentrations exceeding 1 wt.%, except for Ti (precision 4.4%) and Na (accuracy 4.6%). For sulfur, P1326-2 data yield a mean of 1321 ± 74 ppm, close to previously published values (e.g., 1296 ± 26 ppm)[79]. For chlorine, we obtained a mean of 502 ± 123 ppm for Macusanite, in agreement with the GeoRem value of 501 ± 27 ppm[78]. Nevertheless, to account for potential small differences in calibration of the instrument from session to session, we applied a correction factor for Si — the only element present in sufficient concentration for such a correction to be meaningful — based on standard data for each session. These correction factors ($SiO_{2(reference)}$/$SiO_{2(observed)}$) range from 1.000 to 1.020 and are provided in Tables S2 and S4. Using raw or corrected values does not affect the trends observed in the data or the conclusions of the study. Values reported in the main text and figures are corrected sample averages, but individual analyses, as well as sample and daily averages — raw and corrected—are reported Tables S3 and S4.

Image analysis

Backscattered electron (BSE) images and elemental X-ray maps of ash clasts were obtained on a Hitachi scanning electron microscope at Queens College, City University of New York. Then, for 19 representative sample spanning the full eruption sequence and range in SiO_2 content, we used Adobe Illustrator to trace the different phases, which consist of vesicles and microcrysts of plagioclase, clinopyroxene, olivine, Fe-Ti oxides, and, rarely, amphibole, apatite, and sulfides. X-ray maps were used to distinguish phases with similar BSE intensity, particularly clinopyroxene and olivine. We subsequently used ImageJ to obtain the areal fraction of each phase present in ash clasts and calculate the vesicularity and vesicle-free crystallinity of the samples. A representative example is shown in Extended Data Figure 3 and numerical results are provided in Table S5.

Volcanic earthquakes

Two catalogues compile the pre- and syn-eruptive volcano-tectonic seismicity for the 2021 eruption: the publicly available catalogue of the Instituto Geográfico Nacional (IGN) (www.ign.es/web/ign/portal/sis-catalogo-terremotos) and that of the Instituto Volcanológico de Canarias (INVOLCAN)[36]. Both catalogues show a very similar number of events, but differ considerably in reported hypocenter depths[36,38]. Tests performed by Dayton et al.[43] (and outlined in their supplementary materials) indicate that locations of D'Auria et al.[36] are more precise and accurate, mainly due to the choice of seismic velocity model and exclusion of picks from distant (>100 km) seismic stations. We thus

use the earthquake catalogue of D'Auria et al.[36] in our analysis.

Magma ascent rates from the mantle to the lower crust were calculated based on time lags between presumably corresponding mantle and crustal earthquake swarms and the depth difference between the swarms (Fig. 3a). We note that interpretation of hypocenter depths in terms of their spatial relationship with magma bodies is subject to substantial uncertainties[80], as earthquake depths may be coincident with, underestimate, or overestimate the depth of magma. For the 2021 eruption, CO_2 fluid inclusions in olivine suggest the last stages of magma storage were coincident with the depth of the mantle earthquake cluster[43,44], and the crustal cluster may represent a transitory magma stagnation level identified for other eruptions in the Canary Islands[19,81]. For ascent rate calculations, we assumed that the hypocenter–magma depth relationship — whatever it may be — is the same for both the mantle and crustal clusters. Ascent rate is thus obtained by dividing the vertical distance between the earthquake cluster locations (13.9 ± 2.6 km) by the time lag between corresponding mantle and crustal seismic swarms. This yields ascent rates of ~0.01 m/s in October and 0.02–0.03 m/s in November and December (Fig. 3d) (these values increase to 0.02–0.05 m/s when using the deeper hypocenters of the IGN catalogue[38]). Zanon et al.[44] obtained similar results. In comparison, pre-eruptive hypocenter migration yields magma ascent rates of 0.01 and 0.06 m/s at 5–10 and 0–5 km depth, respectively[82].

Volcanic tremor

Tremor amplitude (real-time seismic amplitude measurement, RSAM) data presented in this paper were calculated using continuous seismic waveform data recorded at a triaxial broadband seismic station (PLPI, Llano del Pino) belonging to Red Sísmica Canaria, operated by INVOLCAN. The sampling rate is 100 Hz. This station was selected due to its location — only 3 km south of the eruptive vent — and near-continuous data coverage during the eruption, with gaps of 13, 61, 10, and 43 hours occurring on 14 October, 15–17 October, 2 December, and 5–7 December 2021, respectively. To isolate the tremor contribution to RSAM from discrete earthquake contributions, the raw seismic data were first designaled using the algorithm bc_denoise[83]. The resulting 'denoised' continuous seismic data were then demeaned, detrended, and bandpass-filtered between 0.35–1 Hz and 1–3 Hz, the latter being the most energetic frequency band at PLPI. Hourly RSAM values were then computed and are provided in Table S6.

Tremor locations were calculated using seismic data from the IGN network, which are openly available through FDSN webservices[54].

Estimating the network covariance matrix: Based on refs.[84–86], we applied a network covariance matrix approach to analyze volcanic tremor, using La Palma-based stations of the IGN network ES. We began by processing hour-long data files by detrending and removing the instrument response, then filtered the data between 0.01 and 20 Hz. These data were segmented into 10-minute intervals, referred to as averaging windows. Each averaging window was further divided into 48-second subwindows, within which spectral whitening was applied. Cross spectra were calculated for each subwindow and each possible station combination, creating a covariance matrix by stacking the resulting 50 subwindow covariance matrices for each averaging window. The covariance matrix was decomposed into complex eigenvalues and eigenvectors. We then calculated the spectral width per averaging window, which is a measure of the eigenvalue distribution and presents the number of independent sources, with high values indicating multiple sources (noise) and minimal values indicating a single source.

Spectral width plots were generated using 10-minute averaging window for three key periods: 17–24 September, capturing the eruption onset and highest tremor amplitudes; 15–21 October, representing intermediate tremor amplitudes mid-eruption; and 21–27 November, reflecting lower tremor amplitudes later in the eruption (see Fig. 3a). Additionally, spectral width plots for the entire eruptive period (using hourly averaging windows to decrease computational cost) as well as zooming in on the eruption onset (19 September) and end (13 December) are shown in Extended Data Figure 4.

Automatic tremor localization: We visually inspected spectral width plots to select frequency bands indicative of tremor activity. The 0.35–1 Hz range, which is the strongest and most stable band across the network over different time periods, provided the best-constrained tremor signal. Using the eigenvectors to the dominant eigenvalues, the wavefield was recreated as a cross-correlation function in time using the selected frequency band. This

procedure denoises the data and enhances dominant sources. We used the waveform envelope derived from the Hilbert transform for further analysis and applied minimal Gaussian smoothing of 0.1 s length.

We implemented a 3D grid with a horizontal resolution of 1.1 km and a vertical resolution of 1 km, spanning [28.4°N, -18.05°W to 28.9°N, -17.65°W] and depths from -20 km to 3 km above sea level. Using the 1-D velocity model of ref. [36], we calculated theoretical rays and travel times from each grid point to every station, assuming S-waves. For each grid point, we summed cross-correlation envelopes at differential travel times to generate a spatial likelihood function, normalized by grid volume and maximum likelihood.

Solutions were computed for each time step (10 minutes), with three criteria to identify tremor signals based on: (1) the mean value of the spectral width, which had to be below 0.65, indicating a strong source; (2) the number of grid elements which contain 95% of the maximum likelihood had to be less than 1% of the number of grid elements; and (3) the location was not equal to the boundaries of the grid. A single solution example is shown in Extended Data Fig. 6. Average location errors, based on the 95% threshold, are less than ~3 km horizontally and ~7 km in depth.

Tremor density: We report tremor locations for 515, 820, and 635 10-minute time windows for each respective time periods noted above. Of the 21 days considered, ~18.5 days show tremor, due to some data gaps; this results in ~73% coverage of usable tremor locations.

Since locations cluster spatially, we present tremor density plots in Extended Data Figs. 7–9, showing the total count (n) of located events per grid point. The 0.35–1 Hz tremor almost exclusively locates at shallow depth, very close to the eruption site. Minor discrepancies between the exact position of the eruption site and tremor locations arise due to grid spacing, the nature of cross-correlation functions, and uncertainties in the velocity model.

Viscosity and volatile solubility calculations

Melt viscosities were calculated from matrix glass compositions with the model of Giordano et al.[65], under anhydrous and variably hydrous (up to 3 wt.% H_2O — close to expected values at depth)[61,62] conditions. We used the thermometer of Beattie[66] (see also ref.[87]) obtain input temperatures, which range from 1100 to 1130 °C (Table S7).

The solubility of H_2O and CO_2 as a function of pressure and melt composition was calculated with MagmaSat[88] via the VESIcal code[89]. Calculations were performed for melts with endmember SiO_2 contents from 0.1 to 300 MPa. We used the same temperature inputs as in the melt viscosity calculations and we set the mole fraction of H_2O in the exsolved fluid to 0.4, based on measured gas compositions[61].

Data availability
The datasets[90] generated during this study are available in the EarthChem data repository, http://doi.org/10.60520/IEDA/113537, and in the Supplementary Information.

Methods-only references

77. Stix, J., Gauthier, G. & Ludden, J. N. A critical look at quantitative laser-ablation ICP-MS analysis of natural and synthetic glasses. *The Canadian Mineralogist* **33**, 435–444 (1995).

78. Jochum, K. P. *et al.* GeoReM: A new geochemical database for reference materials and isotopic standards. *Geostandards and Geoanalytical Research* **29**, 333–338 (2005).

79. Longpré, M.-A., Stix, J., Klügel, A. & Shimizu, N. Mantle to surface degassing of carbon- and sulphur-rich alkaline magma at El Hierro, Canary Islands. *Earth and Planetary Science Letters* **460**, 268–280 (2017).

80. Roman, D. C. & Cashman, K. V. Top–down precursory volcanic seismicity: implications for 'stealth'magma ascent and long-term eruption forecasting. *Frontiers in Earth Science* **6**, 124 (2018).

81. Klügel, A., Longpré, M.-A., García-Cañada, L. & Stix, J. Deep intrusions, lateral magma transport and related uplift at ocean island volcanoes. *Earth and Planetary Science Letters* **431**, 140–149 (12AD).

82. Mezcua, J. & Rueda, J. Seismic swarms and earthquake activity b-value related to the September 19, 2021, La Palma volcano eruption in Cumbre Vieja, Canary Islands (Spain). *Bulletin of Volcanology* **85**, 32 (2023).

83. Yang, Y., Liu, C. & Langston, C. A. Processing seismic ambient noise data with the continuous wavelet transform to obtain reliable empirical Green's functions. *Geophysical Journal International* **222**, 1224–1235 (2020).

84. Seydoux, L., Shapiro, N. M., de Rosny, J., Brenguier, F. & Landès, M. Detecting seismic activity with a covariance matrix analysis of data recorded on seismic arrays. *Geophysical Journal International* **204**, 1430–1442 (2016).

85. Soubestre, J. *et al.* Network-based detection and classification of seismovolcanic tremors: Example from the Klyuchevskoy volcanic group in Kamchatka. *Journal of Geophysical Research: Solid Earth* **123**, 564–582 (2018).

86. Soubestre, J. *et al.* Depth migration of seismovolcanic tremor sources below the Klyuchevskoy volcanic group (Kamchatka) determined from a network-based analysis. *Geophysical Research Letters* **46**, 8018–8030 (2019).

87. Putirka, K. D. Thermometers and barometers for volcanic systems. *Reviews in Mineralogy and Geochemistry* **69**, 61–120 (2008).

88. Ghiorso, M. S. & Gualda, G. A. R. An H_2O–CO_2 mixed fluid saturation model compatible with rhyolite-MELTS. *Contributions to Mineralogy and Petrology* **169**, 1–30 (2015).

89. Iacovino, K., Matthews, S., Wieser, P. E., Moore, G. M. & Bégué, F. VESIcal Part I: An open-source thermodynamic model engine for mixed volatile (H_2O-CO_2) solubility in silicate melts. *Earth and Space Science* **8**, e2020EA001584 (2021).

90. Longpré, M.-A., Tramontano, S., Pankhurst, M. J. Daily time series of matrix glass composition from tephra samples from the 2021 Tajogaite eruption at Cumbre Vieja volcano (La Palma, Canary Islands), Version 1.0. Interdisciplinary Earth Data Alliance (IEDA). http://doi.org/10.60520/IEDA/113537. Accessed 2024-11-12 (2024).
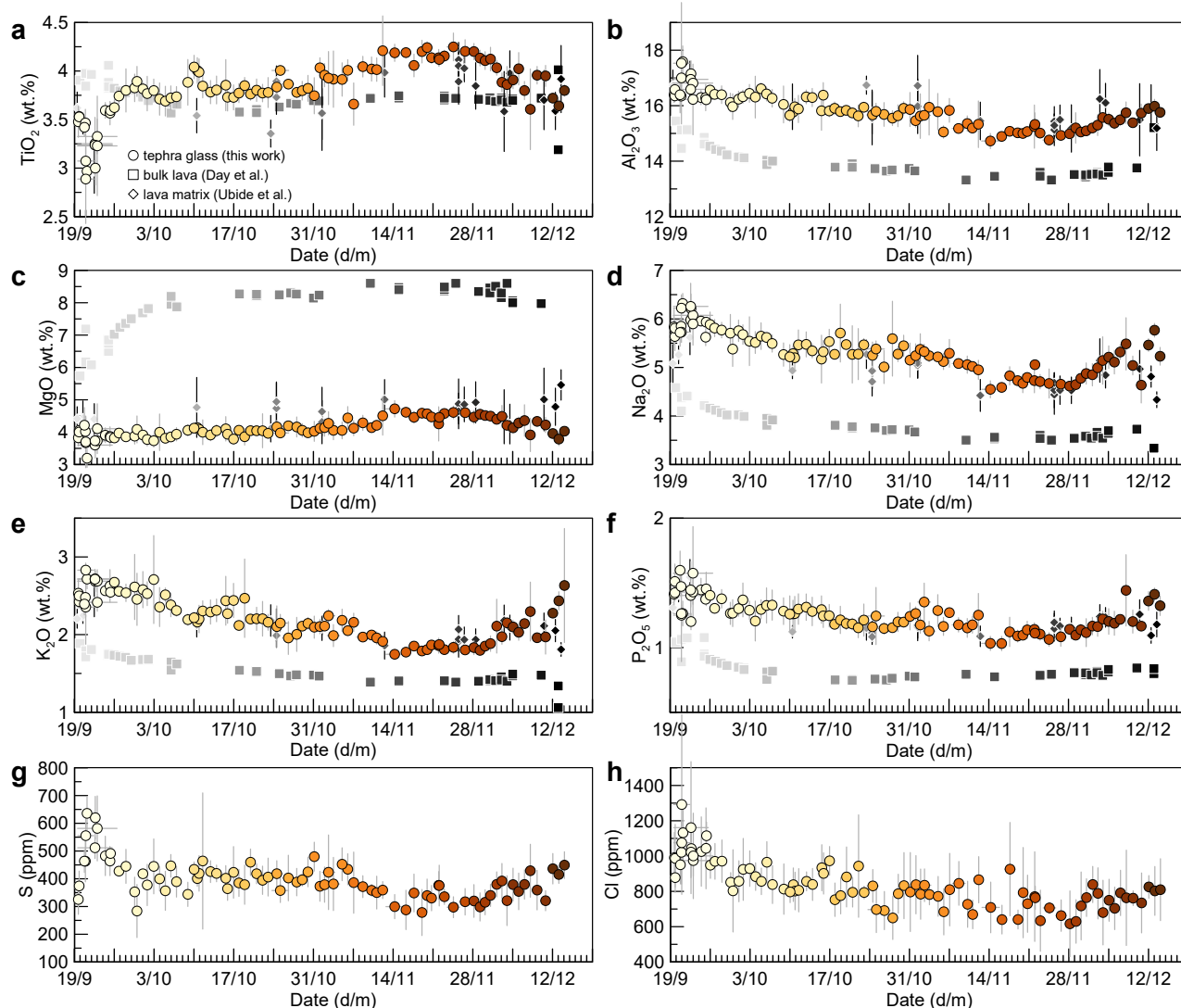
Extended Data Figure 1. Glass composition time series. (a) TiO_2, (b) Al_2O_3, (c), MgO, (d) Na_2O, (e) K_2O, (f) P_2O_5, (g) S and (h) Cl concentrations as a function of time. Bulk rock data are from Day et al.[28] and lava matrix data are from Ubide et al.[42]. Note the strong decoupling of glass and bulk rock data for some elements (e.g., Ti, Mg, Na), particularly in the first week and last two weeks of the eruption. Vertical gray error bars show one standard deviation based on 3–13 analyses on at least two ash clasts per sample, whereas horizontal error bars indicate the ash sampling timespan. Error bars are not shown when smaller than symbol size. Black error bars for lava matrix data are one standard deviation from 7–10 analyses[42].
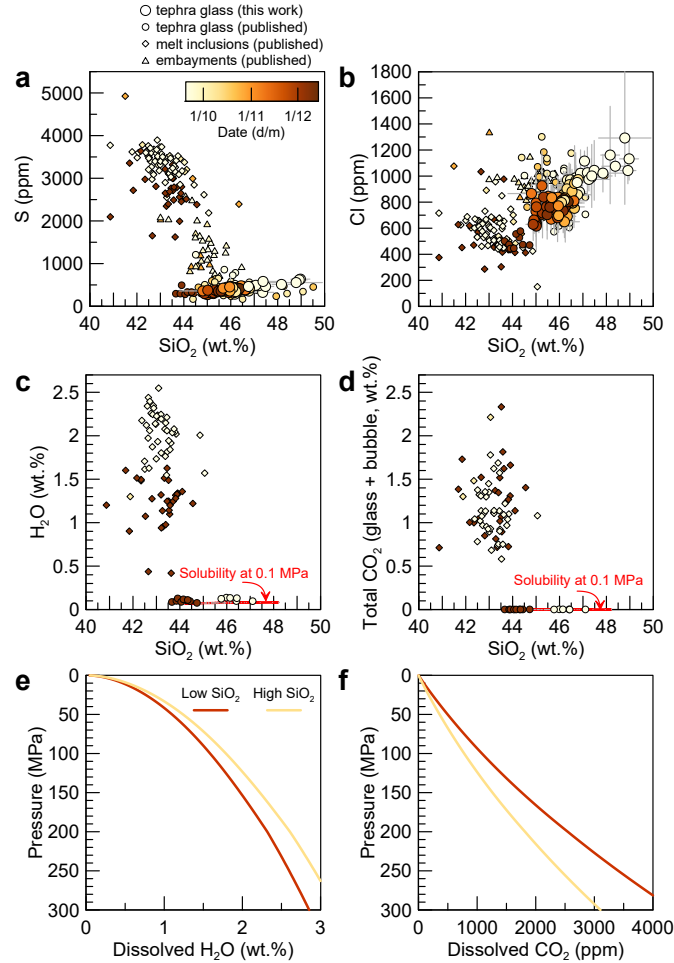
Extended Data Figure 2. Volatile elements. (a) Sulfur and (b) chlorine concentrations (ppm) vs. SiO_2 in our tephra glass samples, compared with published data on melt inclusions, embayments, and tephra glasses[61,62]. Data from this work are presented as means of 3–13 analyses on at least two ash clasts per sample, with gray error bars displaying one standard deviation. Sulfur in tephra glasses (280–640 ppm S) is much lower than in melt inclusions due to extensive degassing, whereas chlorine (620–1290 ppm) shows incompatible behavior and little to no degassing. (c) H_2O and (d) total (glass + bubble) CO_2 contents in melt inclusions and tephra glasses. Data from Dayton et al.[62]. A sample from the first few days of the eruption shows higher H_2O (but similar CO_2) than a late-stage sample approximately dated to December 2021. Solubility at 0.1 MPa (1 bar) is shown as a red line. (e) H_2O and (f) CO_2 solubility as a function of pressure for low- and high-SiO_2 melt endmembers. All volatile solubility calculations were performed using MagmaSat[88] via VESIcal[89], assuming a mole fraction of H_2O in the fluid of 0.4 (ref. [61]) (Methods).
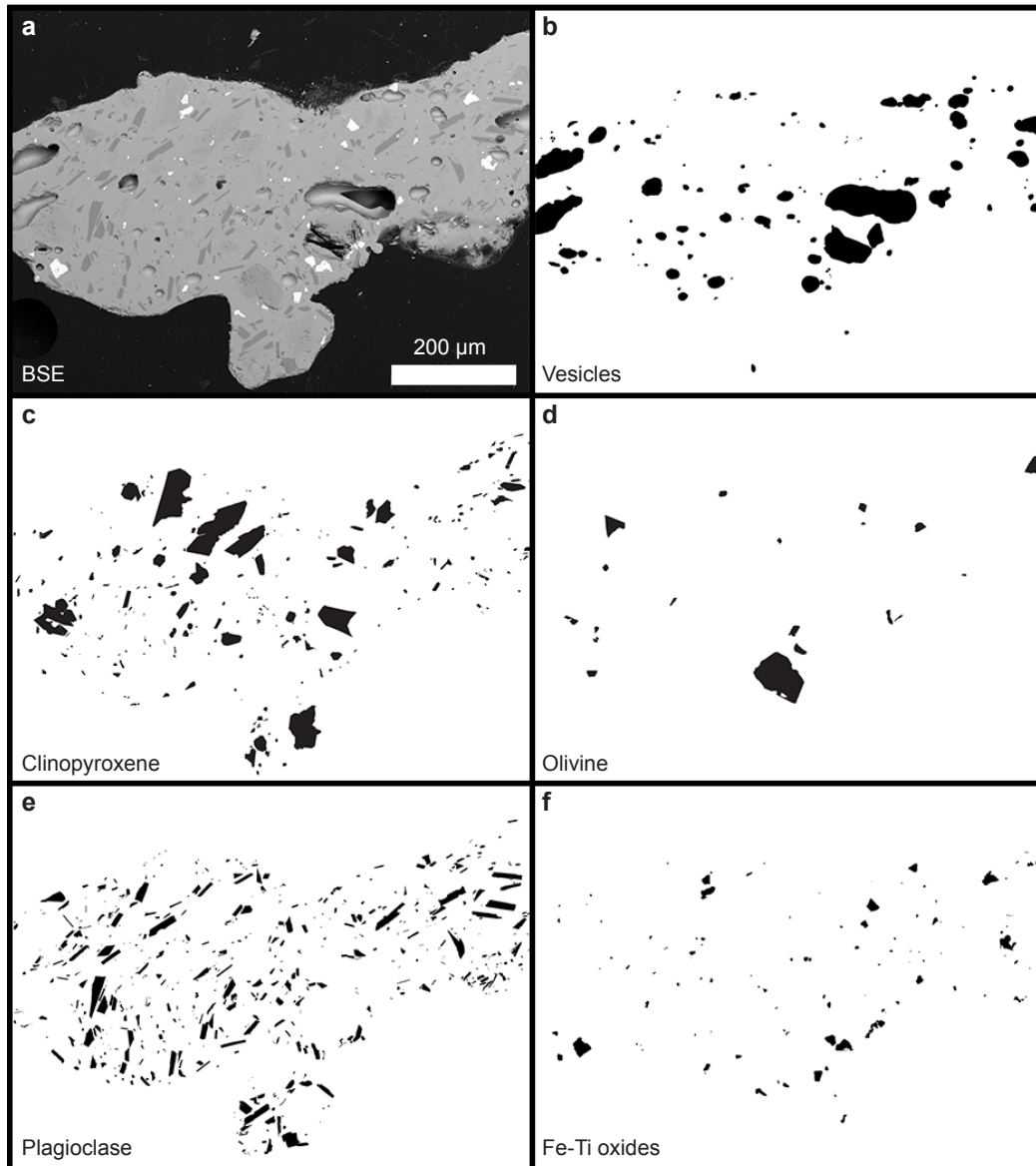
Extended Data Figure 3. Image analysis example for crystallinity and vesicularity estimates. (a) Backscattered electron image of a representative Type A ash clast from sample CAN-TLP-0212. (b–f) Traced amounts of vesicles, clinopyroxene, olivine, plagioclase, and Fe-Ti oxides used to calculate vesicularity and crystallinity. For this sample, we obtain a vesicularity of 11.0 vol.% and a vesicle-free crystallinity of 25.6 vol.% (Cpx: 11.2 vol.%; Plag: 9.5 vol.%; Ol: 2.9 vol.%; Ox: 2.0 vol.%).
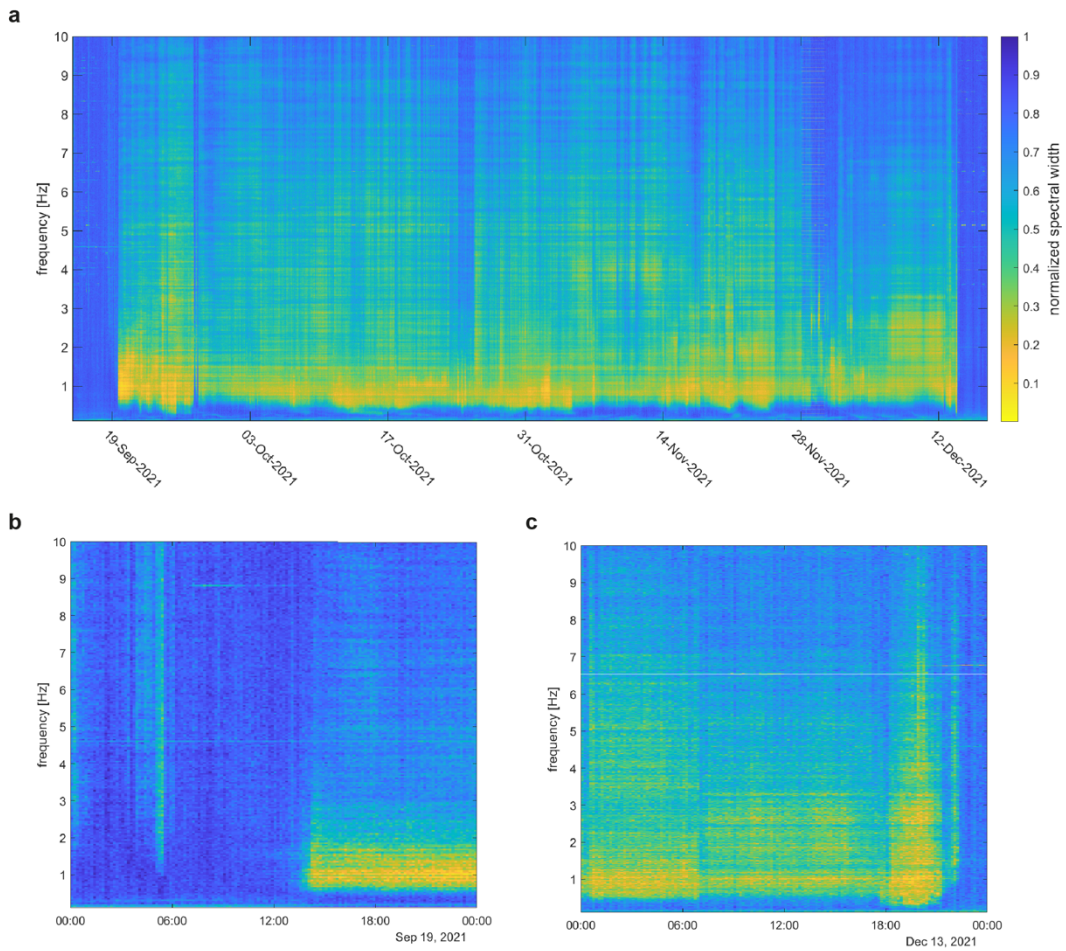
Extended Data Figure 4. Spectral width for seismic stations from the IGN network. Panel (a) shows the whole eruption period, whereas (b) and (c) respectively focus on the onset and end of the tremor signal on 19 September and 13 December.
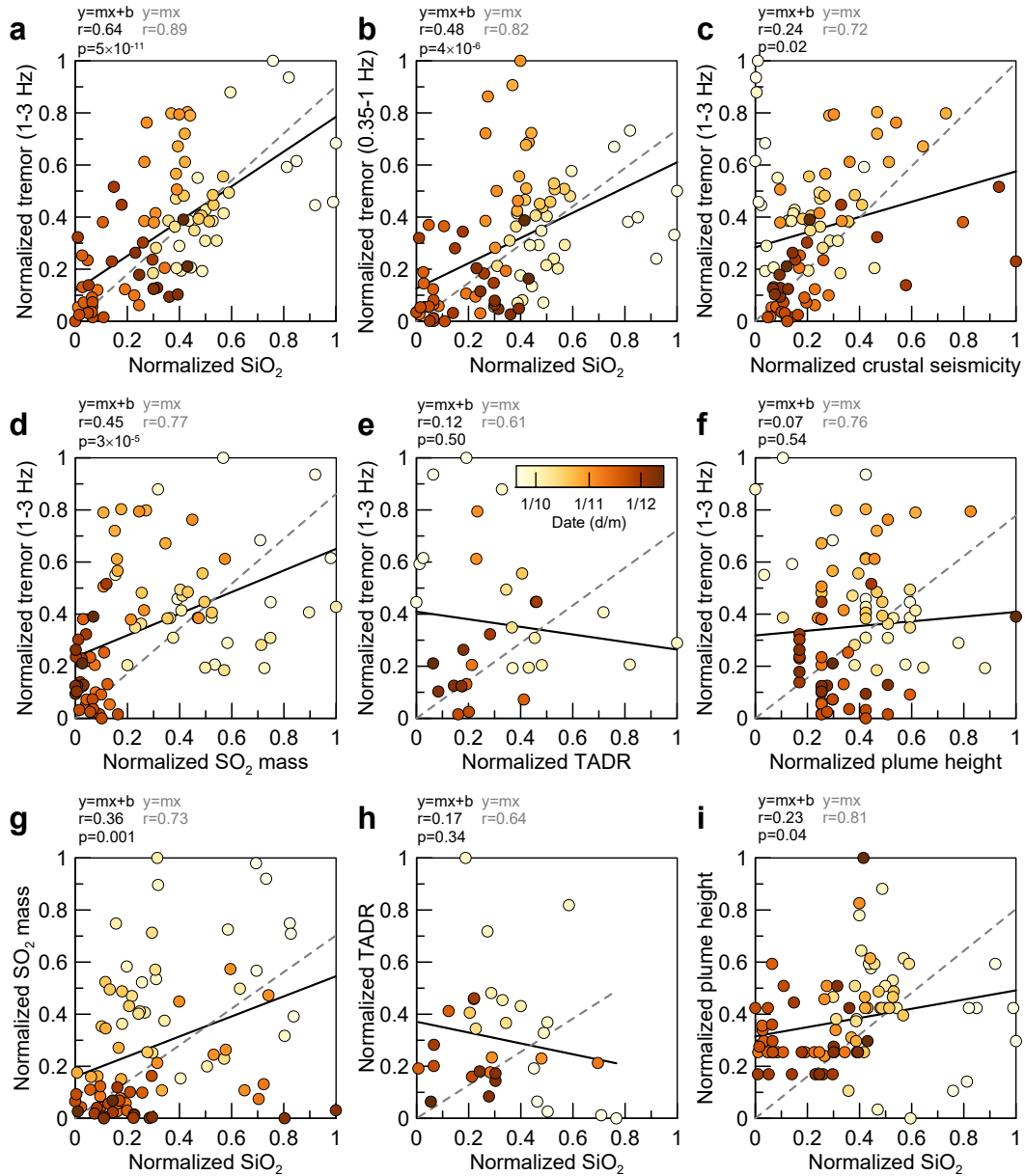
Extended Data Figure 5. Regression analysis and supplementary monitoring data. Regression analysis for resampled (daily averages) and normalized time series of tremor amplitude at station PLPI in the (a) 1–3 Hz and (b) 0.35–1 Hz bands versus melt SiO_2 content, and 1–3 Hz versus (c) number of discrete earthquakes in the crustal cluster[36], (d) SO_2 mass[60], (e) TADR[59], and (f) ash plume height[63]. Panels (g–i) respectively show SO_2 mass, TADR, and ash plume height against SiO_2 content. Solid black lines are linear best-fits through the data, with associated correlation coefficient (r) and p-value in black font. Data analysis is based on the two-sided t-test. Dashed gray lines are fits forced through the origin, with associated r in gray font.
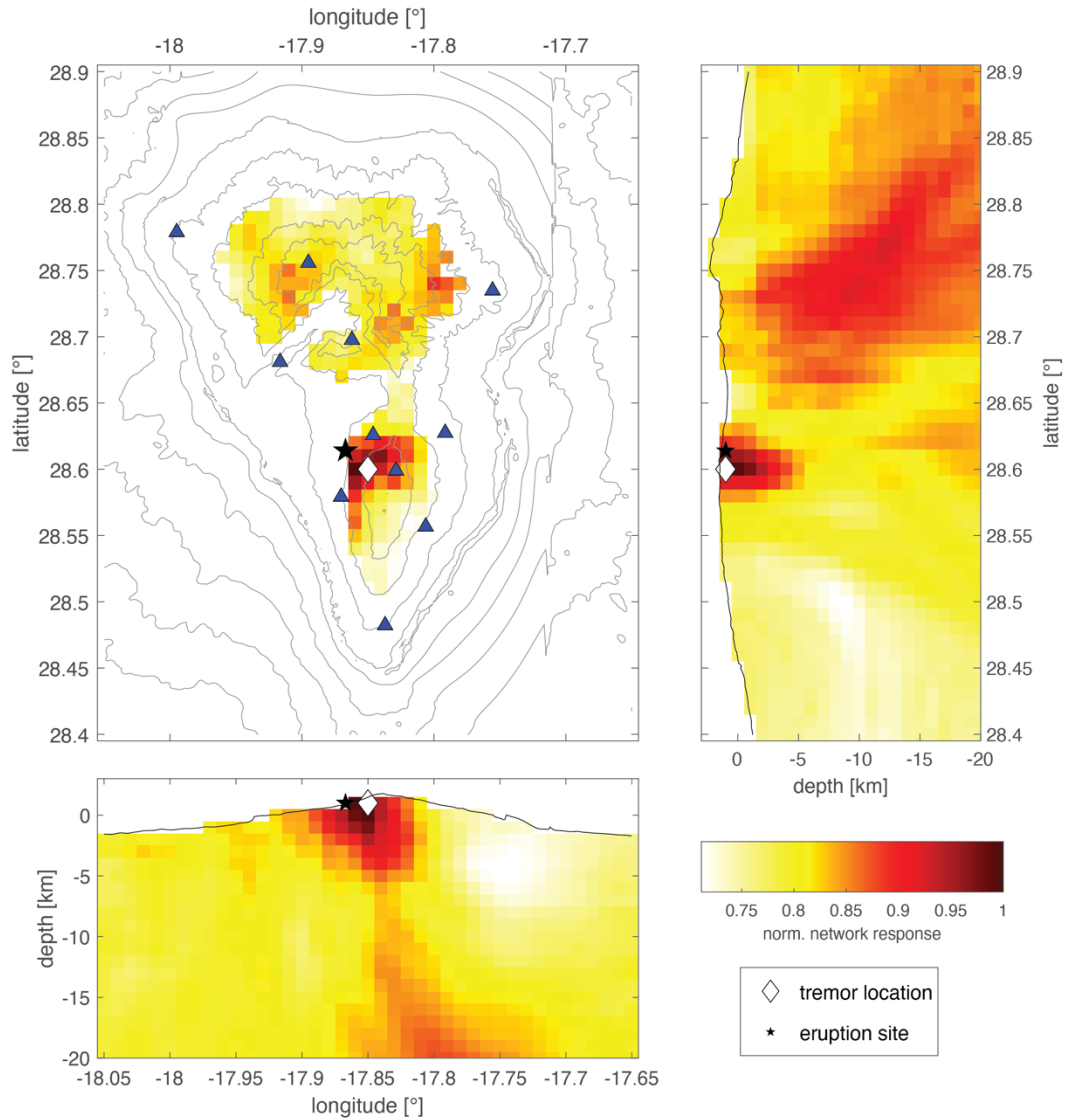
Extended Data Figure 6. Single solution for a tremor location for the onset of the eruption on 19 September 2021, 13:50. Blue triangles show seismic stations that were utilized. Colors denote the network response (white to dark red showing small to large values). The white diamond corresponds to the highest network response, which we infer is the location of the tremor, and the black star is the eruption site.
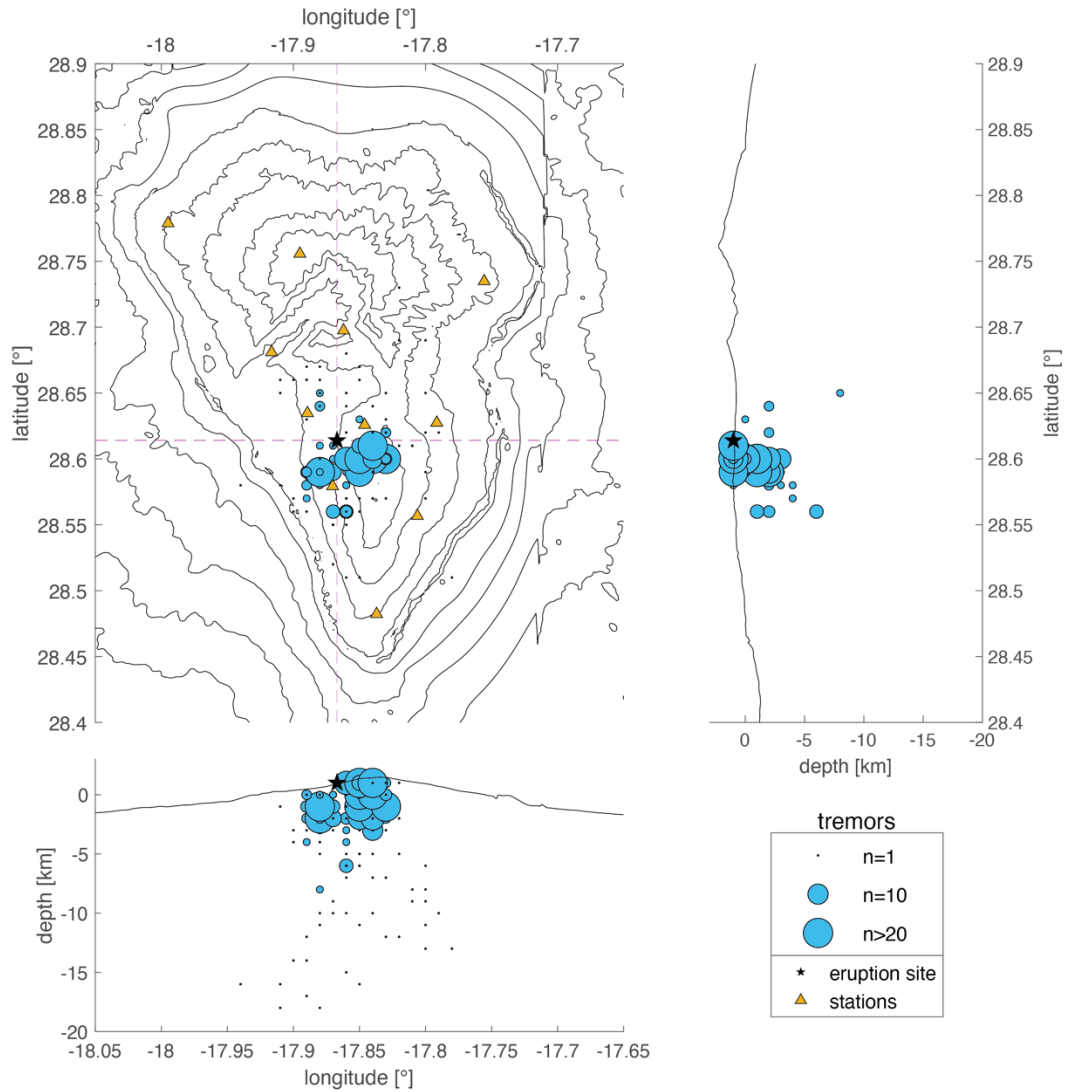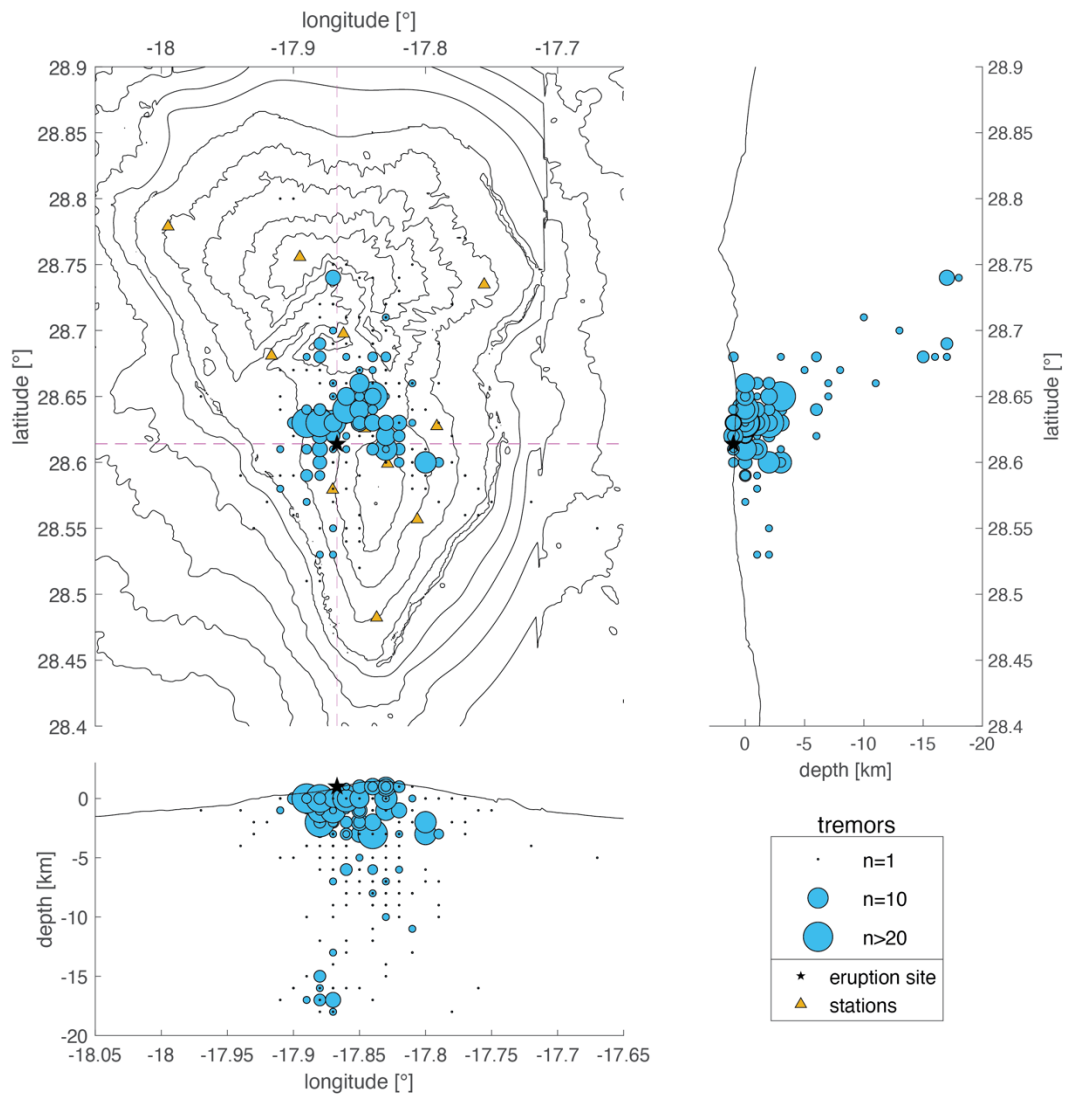
Extended Data Figure 7. Tremor locations for 17–24 September 2021. Cyan circles indicate tremor density, where the size of the circle corresponds to the number of tremors (n) locating at that grid point. Yellow triangles show seismic stations and the black star shows the eruption site.
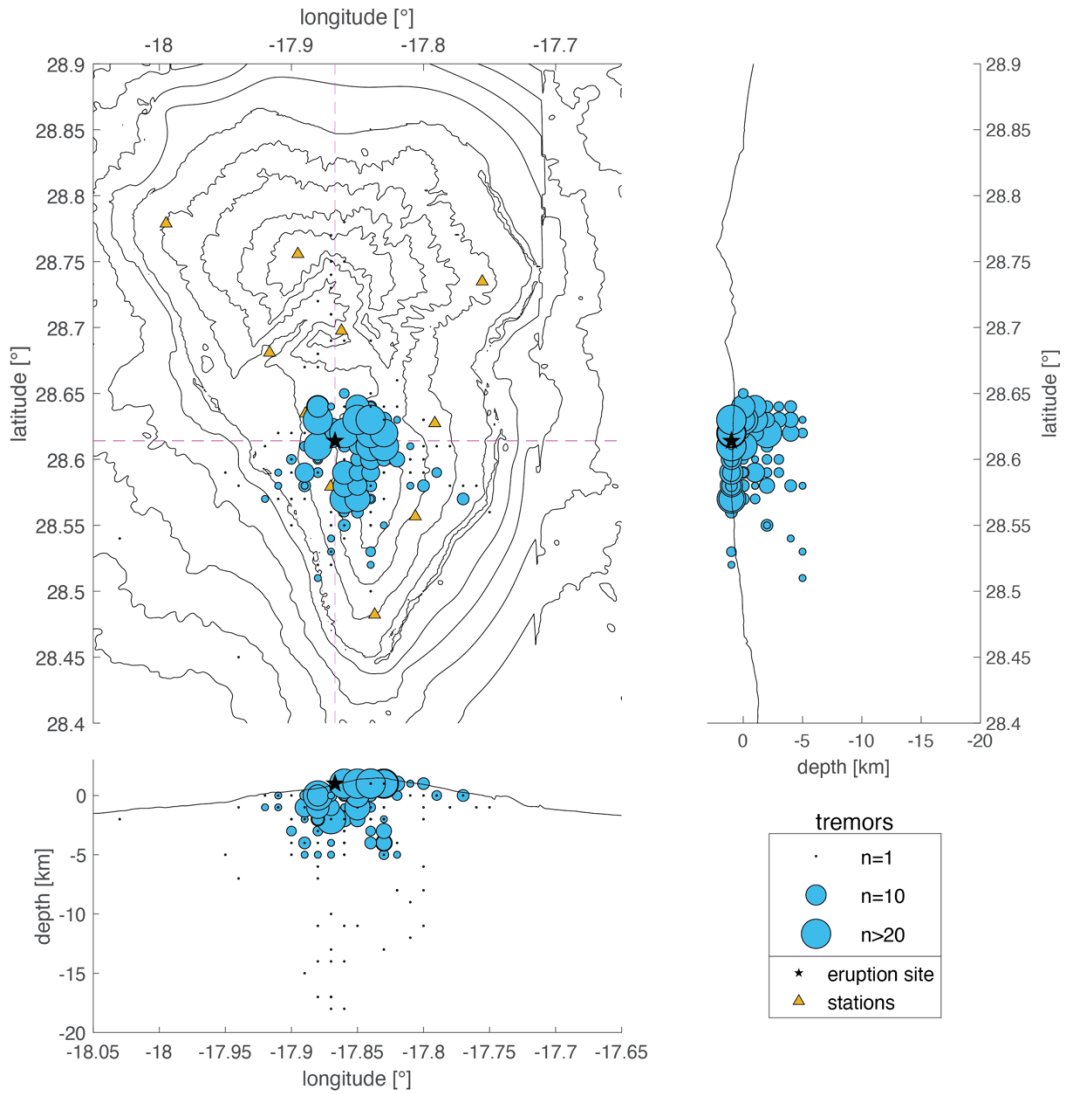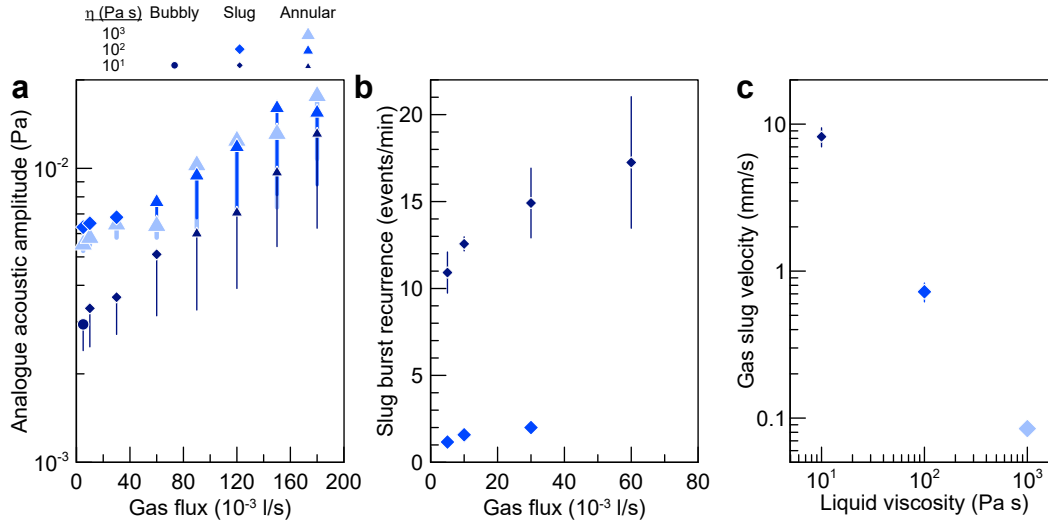
Extended Data Figure 8. Tremor locations for 15–21 October 2021. Symbols as in Extended Data Fig. 7.

Extended Data Figure 9. Tremor locations for 21–27 November 2021. Symbols as in Extended Data Fig. 7.

Extended Data Figure 10. Experimental evidence for the effects of liquid viscosity. (a) Amplitude of analogue acoustic signal as a function of gas flux in laboratory experiments[56]. Symbols mark the average 75th percentile values for three experiments (230–525 observations per experiment, over 46–105 s using a 0.2 s sliding window) conducted with different conduit roughness, with downward error bars showing the average interquartile range. Symbols are color-coded according to liquid viscosity (η) of the experiments and symbol shape indicates the observed flow regime (bubbly, slug, or annular, see Fig. 5a). (b) Recurrence rate of gas slug burst events vs. gas flux. (c) Slug ascent velocity against liquid viscosity. Both (b) and (c) show experiments in the slug regime only, with data presented as means ± one standard deviation (not shown when smaller than symbol) of three experimental runs conducted with varying conduit roughness.